Cell Reports

Report

The NLRP3 inflammasome in microglia regulates repetitive behavior by modulating NMDA glutamate receptor functions

Graphical abstract

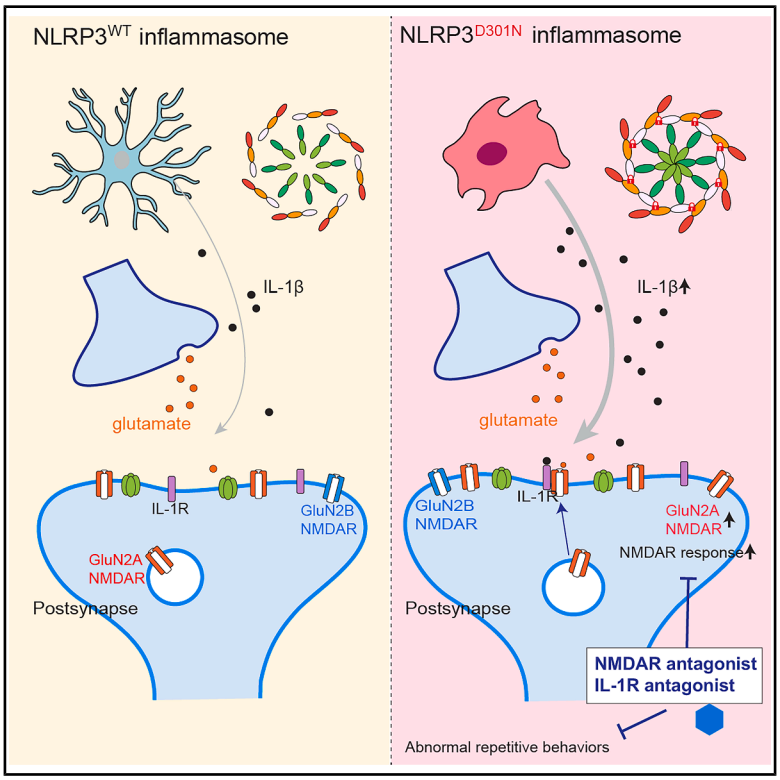

Highlights

- NLRP3-mediated neuroinflammation alters excitatory synaptic density and NMDAR function
- NLRP3-mediated neuroinflammation induces abnormal anxiety-like and repetitive behaviors
- IL-1β induces NMDAR hyperactivation by altering the surface levels of NMDAR subunits
- Antagonizing IL-1R and hyperactivated NMDAR reverses abnormal repetitive behavior

Authors

Hyeji Jung, Byeongchan Kim, Gyubin Jang, ..., Jaewon Ko, Je-Wook Yu, Ji Won Um

Correspondence

jiwonum@dgist.ac.kr

In brief

In this study, Jung et al. investigate the effect of excessive NLRP3-mediated neuroinflammation on synaptic functions and behaviors using *Nlrp3*^{D301N}-conditional knockin mice. Strikingly, excessive NLRP3-mediated neuroinflammation causes NMDAR hyperactivation, leading to abnormal behaviors. Treatment with IL-1β receptor antagonist (IL-1RA) or NMDAR antagonist reverses the pathological phenotypes.

Jung et al., 2025, Cell Reports *44*, 115656
May 27, 2025 © 2025 The Author(s). Published by Elsevier Inc.
https://doi.org/10.1016/j.celrep.2025.115656

CellPress

Cell Reports

CellPress
OPEN ACCESS

Report

The NLRP3 inflammasome in microglia regulates repetitive behavior by modulating NMDA glutamate receptor functions

Hyeji Jung,[1,2] Byeongchan Kim,[1] Gyubin Jang,[1,2] Hyeonho Kim,[1,2] Ae-Ree Lee,[3,4] Sung-Hyun Yoon,[5] Kyung-Seo Lee,[5] Gaeun Hyun,[1] Younghye Kim,[1,2] Jaewon Ko,[1,2] Je-Wook Yu,[5] and Ji Won Um[1,2,6,*]

[1]Department of Brain Sciences, Daegu Gyeongbuk Institute of Science and Technology (DGIST), 333 Techno Jungangdae-Ro, Hyeonpoong-Eup, Dalseong-Gun, Daegu 42988, Korea

[2]Center for Synapse Diversity and Specificity, DGIST, 333 Techno Jungangdae-Ro, Hyeonpoong-Eup, Dalseong-Gun, Daegu 42988, Korea

[3]Core Protein Resources Center, DGIST, Daegu 42988, Korea

[4]iProteinTherapeutics (iPT), Daegu 42988, Korea

[5]Department of Microbiology and Immunology, Institute for Immunology and Immunological Diseases, Brain Korea 21 PLUS Project for Medical Science, Yonsei University College of Medicine, Seoul 03722, Korea

[6]Lead contact

*Correspondence: jiwonum@dgist.ac.kr

https://doi.org/10.1016/j.celrep.2025.115656

SUMMARY

Neuroinflammation is a well-established risk factor for various neurological disorders and cognitive decline. However, the precise molecular mechanisms linking inflammation with neuropsychiatric symptoms remain unclear. Here, using NLRP3 (NOD-like receptor family, pyrin domain-containing protein 3) conditional knockin (cKI) mice harboring a D301N point mutation originating in patients with autoinflammatory diseases, we found that activation of the NLRP3 inflammasome by administration of lipopolysaccharide induced anxiety-like and repetitive behaviors frequently found in patients with neuropsychiatric disorders, as well as increasing NMDAR (N-methyl-D-aspartate receptor)-mediated excitatory synaptic functions in the medial prefrontal cortex of mice. In addition, interleukin 1β (IL-1β), a downstream cytokine of the NLRP3 inflammasome, enhanced NMDAR activation and increased surface levels of the selective NMDAR subunit GluN2A in cultured cortical neurons. Strikingly, treatment with an NMDAR antagonist or IL-1 receptor antagonist completely normalized the specific behavioral deficits in *Nlrp3*^{D301N}-cKI mice. Collectively, our results demonstrate that NLRP3-mediated neuroinflammation elicits repetitive behavior through impaired NMDAR functions.

INTRODUCTION

Inflammasome-mediated neuroinflammatory responses are of considerable importance in the pathological progression of neurological diseases.[1,2] Recently, mounting evidence has suggested that improper immune function contributes to neuropsychiatric symptoms.[3,4] Chronic inflammation is reported to be involved in posttraumatic stress disorder, anxiety, and major mood disorders.[5,6] Clinically, ~40% of patients with systemic inflammation triggered by a dysregulated host response to infection (e.g., sepsis) exhibit mild-to-moderate residual neuropsychiatric symptoms, including depression, anxiety, or cognitive disturbances.[7] It has also been shown that individuals with anxiety and depression have elevated serum concentrations of pro-inflammatory cytokines, such as tumor necrosis factor alpha (TNF-α), interleukin 1β (IL-1β), IL-6, and interferon γ.[8,9] However, the molecular mechanisms underlying the link between inflammation and neuropsychiatric symptoms remain unexplored.

The NLRP3 (NOD-like receptor [NLR] family, pyrin domain-containing protein 3) inflammasome is strongly implicated in the connection between central and peripheral inflammation and various neurodegenerative diseases, including Alzheimer's disease (AD) and Parkinson's disease,[10–12] as well as mood disorders such as anxiety and major mood disorder.[13–15] Upon stimulation of danger-associated molecular patterns (DAMPs), such as adenosine triphosphate, NLRP3 recruits ASC (apoptosis-associated speck-like protein containing a CARD domain) to form the inflammasome, resulting in increased production of mature IL-1β.[16] IL-1β initiates multiple inflammatory pathways, modulating neuronal excitability and behavioral responses in mice.[17,18] Moreover, the microglial NLRP3-mediated inflammasome plays a role in regulating neuronal cell death and fear memory formation through microglial activation[19,20] and regulating depression-like behavior through activation of A1-like astrocytes.[14] In addition, hyperactivation of the NLRP3 inflammasome through a D301N gain-of-function mutation, associated with an inherited autoinflammatory disease,[21] directly

This is an open access article under the CC BY-NC-ND license (http://creativecommons.org/licenses/by-nc-nd/4.0/).

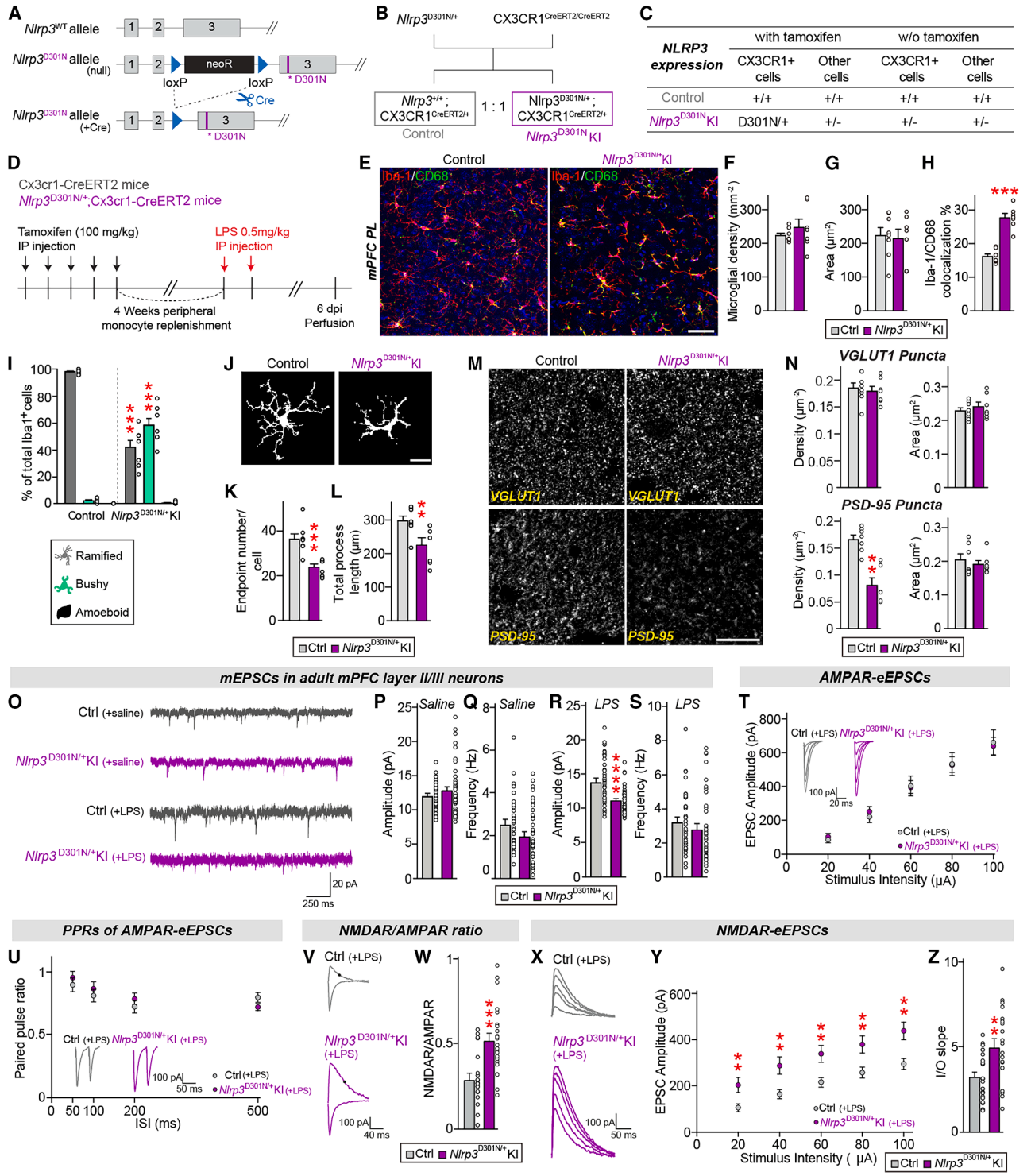

Figure 1. *Nlrp3*^{D301N}-cKI mice exhibit long-lasting inflammation and altered excitatory synaptic function

(A) Strategy used to generate Nlrp3^{D301N}-cKI mice. Arrows flanking the neomycin-resistant (NeoR) gene indicate *loxP* sites. Gray boxes indicate exons.

(B) Mouse breeding strategy.

(C) Summary table showing cell-type-specific *Nlrp3* gene expression in control and *Nlrp3*^{D301N}-cKI mice with or without tamoxifen treatment.

(D) Schematic illustration of the experimental procedure.

(E) Representative images of mPFC regions of control and *Nlrp3*^{D301N}-cKI mice, immunostained for Iba-1 (red) and CD68 (green). Scale bars: 50 μm.

(F and G) Quantification of the density (F) or size (G) of Iba-1^{+} cells.

(legend continued on next page)

impairs hearing in mice.[22] The murine NLRP3 D301N mutation corresponds to the human NLRP3 D303N mutation, which originated from patients with autoinflammatory diseases. This residue is located within the NACHT domain of NLRP3, and its mutation results, presumably through a conformational change, in a constitutively activated inflammasome that exaggerates inflammatory responses.[23]

Although the NLRP3 inflammasome has been clearly linked to certain pathologies of neurological diseases, it remains unclear how its malfunction alters synaptic functions and causes behavioral abnormalities independent of other preceding and overriding pathologies. In the current study, we utilized a conditional knockin (cKI) mouse model in which NLRP3 D301N is specifically expressed in microglia, in conjunction with imaging, electrophysiology, and behavioral analyses, to elucidate the mechanisms underlying NLRP3 inflammasome-induced cellular and synaptic alterations. We showed that microglia-specific *Nlrp3*^{D301N}-cKI mice exhibit increased N-methyl-D-aspartate receptor (NMDAR)-mediated excitatory synaptic transmission and anxiety-like and repetitive behaviors. In addition, we found that normalization of hyperactive NMDAR functions rescued these behavioral deficits in microglia-specific *Nlrp3*^{D301N}-cKI mice. Taken together, our findings illustrate the specific microglial actions of the NLRP3 inflammasome in the regulation of selective excitatory synaptic properties in neurons and the modulation of specific behavioral manifestations.

RESULTS

Microglia-specific *Nlrp3*^{D301N}-cKI mice displayed long-lasting microglial activation

To avoid the deleterious effects of the NLRP3 mutation on peripheral immune systems, we generated a mouse model that conditionally expresses the NLRP3 D301N point mutant in CX3CR1^{+} microglia upon tamoxifen injections (Figures 1A–1C). We conducted all experiments beginning 4 weeks after the last tamoxifen administration to allow repopulation of peripheral bone marrow-derived *Cx3cr1*-CreERT2-expressing cells (e.g., monocytes) (Figure 1D). To investigate whether mice with microglia-specific expression of NLRP3 D301N exhibit extensive neuroinflammation upon lipopolysaccharide (LPS) injection, we performed an immunohistochemical assessment of the numbers of microglia positive for the microglial marker Iba-1 (ionized calcium-binding adapter molecule-1) and expression levels of the lysosomal protein CD68, a marker for actively phagocytic microglia, at 6 days post-LPS injection (dpi). We found a significant increase in the microglial activation at 6 dpi in the medial prefrontal cortex (mPFC) of *Nlrp3*^{D301N}-cKI mice compared with control mice (Figures 1E–1H), as assessed by the colocalization percentage of Iba-1 and CD68. We then analyzed the morphology of microglia, which correlates well with their activation status.[24] Immunohistochemical analyses revealed that microglia in control mice primarily exhibited ramified morphology at 6 dpi, whereas microglia from *Nlrp3*^{D301N}-cKI mice exhibited a change from a ramified to a bushy morphology (Figure 1I). Additional analyses revealed a significant decrease in the number of microglia endpoints and the total length of microglia processes at 6 dpi in *Nlrp3*^{D301N}-cKI mice compared with control mice (Figures 1J–1L). All these changes observed in LPS-treated *Nlrp3*^{D301N}-cKI mice were absent in saline-treated *Nlrp3*^{D301N}-cKI mice and did not involve any increase of immune cell infiltration or cytokine levels (Figure S1), suggesting that baseline inflammation was comparable in *Nlrp3*^{D301N}-cKI mice and control mice in the absence of LPS treatment. In the hippocampal CA1 area, microglia numbers and CD68 expression were markedly increased at 6 dpi in *Nlrp3*^{D301N}-cKI mice, and microglial morphology was altered toward bushy forms (Figures S2A–S2F). Similar to results obtained in the mPFC region, both the number of endpoints and the total length of microglial processes in the hippocampal CA1 area were markedly decreased in the *Nlrp3*^{D301N}-cKI mice (Figures S2G–S2I). Astrocyte activation was observed in mPFC regions of *Nlrp3*^{D301N}-cKI mice at 6 dpi but not in hippocampal CA1 regions, as determined by immunostaining with an anti-GFAP antibody (Figures S2J–S2M). This indicates that the excessive NLRP3 inflammasome-mediated neuroinflammation was indirectly accompanied by astrogliosis.

Excessive NLRP3-dependent inflammation reduces glutamatergic synapse density in the mPFC of adult mice

Next, to investigate whether excessive NLRP3-mediated microglial activation contributes to synaptic alterations, we analyzed excitatory and inhibitory synaptic puncta in the mPFC of LPS-injected mice at 6 dpi. Quantitative immunofluorescence analyses

(H) Quantification of the colocalization percentage of Iba-1^{+}/CD68^{+} cells.
(I) Percentage of microglia displaying a ramified, bushy, or ameboid morphology.
(J) Representative binary images of Iba-1 staining in mPFC regions. Scale bars: 20 μm.
(K and L) Quantification of the number of Iba-1^{+} cell process endpoints (K) or the total lengths of Iba-1^{+} cell processes (L).
(M) Representative images of mPFC regions of control and *Nlrp3*^{D301N}-cKI mice, immunostained for VGLUT1 or PSD-95. Scale bar: 20 μm.
(N) Quantification of the density and size of VGLUT1^{+} or PSD-95^{+} synaptic puncta.
(O) Representative traces of mEPSCs recorded from layer 2/3 pyramidal neurons in the mPFC of control and *Nlrp3*^{D301N}-cKI mice 6 days after saline or LPS treatment.
(P–S) Quantification of the amplitude (P and R) and frequency (Q and S) of mEPSCs recorded from control and *Nlrp3*^{D301N}-cKI mice treated with saline (P and Q) or LPS (R and S).
(T) Excitatory synaptic strength, measured using input-output (I-O) curves, depicted as representative AMPAR-eEPSC traces and summary plots of EPSC amplitudes.
(U) Representative trace of EPSC paired-pulse ratios (PPRs) at an interstimulus interval of 50 ms and summary plots of EPSC PPRs.
(V and W) Representative traces (V) and summary graphs (W) of NMDAR/AMPAR EPSC ratios.
(X–Z) Representative traces (X), summary plots of the NMDAR-eEPSC amplitudes as a function of stimulation current (Y), and a summary graph of fitted linear I-O slopes (Z).

showed that the density and average puncta size of the excitatory presynaptic marker VGLUT1 (vesicular glutamate transporter 1) were unchanged, but the puncta density of the excitatory postsynaptic marker PSD-95 (postsynaptic density 95) was significantly reduced in mPFC regions of *Nlrp3*^{D301N}-cKI mice (Figures 1M and 1N). The density and average size of puncta positive for the inhibitory presynaptic marker VGAT (vesicular GABA transporter) and inhibitory postsynaptic marker $GABA_AR\gamma2$ were unchanged (Figures S3A–S3E), despite a trend toward a reduction in the density of inhibitory postsynapses. Semi-quantitative immunoblot analyses showed that the relative expression levels of synaptic proteins in *Nlrp3*^{D301N}-cKI mouse brains were unchanged (Figures S3F and S3G), suggesting that the reduction of PSD-95$^+$ synaptic puncta was not attributable to any alteration of total protein levels. Meanwhile, TUNEL$^+$ apoptotic nuclei were barely detectable in the mPFC (data not shown), suggesting that the reduction in PSD-95 puncta density is not attributable to neuronal death following intensive neuroinflammation within the mPFC.

Similarly, the density and size of excitatory and inhibitory presynaptic synapses were unchanged in all examined layers of the hippocampal CA1, including the *stratum oriens* (SO), *stratum radiatum* (SR), *stratum pyramidale*, and *stratum lacunosum moleculare*, at 6 dpi in LPS-injected *Nlrp3*^{D301N}-cKI mice (Figures S3H–S3K). In contrast, the density and average size of both excitatory and inhibitory post-synapses were significantly decreased in the SO or SR layer of the hippocampal CA1 at 6 dpi in these mice (Figures S3H–S3K). These data indicate that excessive neuroinflammation mediated by the NLRP3 inflammasome specifically induces alterations in the number and size of excitatory synapses, especially excitatory post-synapses, at 6 dpi in LPS-injected *Nlrp3*^{D301N}-cKI mice.

NMDAR-mediated excitatory synaptic strengths are altered in the mPFC in the context of excessive NLRP3-dependent inflammation

To corroborate the results of anatomical analyses, we next measured miniature excitatory postsynaptic currents (mEPSCs) and miniature inhibitory postsynaptic currents (mIPSCs) in mPFC pyramidal neurons of LPS-injected control and *Nlrp3*^{D301N}-cKI mice at 6 dpi using whole-cell electrophysiological recordings. The amplitude, but not the frequency, of mEPSCs was markedly decreased in mPFC pyramidal neurons of LPS-treated *Nlrp3*^{D301N}-cKI mice (Figures 1O, 1R, and 1S). The reduction in mEPSC amplitude observed in LPS-treated *Nlrp3*^{D301N}-cKI mice was not attributable to genotype because there was no difference in the amplitude of mEPSCs in saline-treated *Nlrp3*^{D301N}-cKI mice compared with saline-treated control mice (Figures 1P and 1Q). In contrast, the amplitude and frequency of mIPSCs were unchanged (Figures S3L and S3M), in line with the anatomical results. In addition, the amplitude and paired-pulse ratio of evoked EPSCs (eEPSCs) in *Nlrp3*^{D301N}-cKI mice were comparable to those in control mice (Figures 1T and 1U) with slightly increased excitability and resting membrane potential (Figures S3N–S3P).

We next measured the ratio of AMPAR (α-amino-3-hydroxy-5-methyl-4-isoxazolepropionic acid receptor)- and NMDAR-mediated eEPSCs (NMDAR/AMPAR ratio) through whole-cell recordings. Intriguingly, the NMDAR/AMPAR ratio of eEPSCs was significantly increased (∼79.42%) in *Nlrp3*^{D301N}-cKI mice compared with control mice (control, 0.29 ± 0.04; *Nlrp3*^{D301N}-cKI, 0.52 ± 0.04) (Figures 1V and 1W), suggesting that excessive NLRP3-mediated neuroinflammation leads to an altered NMDAR/AMPAR ratio. The elevated NMDAR/AMPAR ratio of eEPSCs in *Nlrp3*^{D301N}-cKI mice, despite normal basal transmission, which is mainly mediated by AMPARs, suggested that the amplitude of NMDAR-mediated eEPSCs was likely increased. In line with this conjecture, we found that the amplitude of NMDAR-eEPSCs was indeed significantly increased in *Nlrp3*^{D301N}-cKI mice compared with control mice (Figures 1X–1Z). Collectively, these results suggest that excessive NLRP3-mediated neuroinflammation influences the NMDAR-mediated postsynaptic responses.

Microglial phagocytic elimination of synapses is not responsible for the decreased number of excitatory synapses

Microglia-mediated phagocytic activity is essential for synapse pruning and the elimination of dead cells.[25] Thus, we decided to examine whether the reduced number of excitatory synapses observed in *Nlrp3*^{D301N}-cKI mice is attributable to microglial engulfment. To this end, we used an immunofluorescence analysis to evaluate the number of PSD-95$^+$ puncta within the Iba-1$^+$CD68$^+$ microglia lysosome in hippocampal CA1 and mPFC regions. Confocal imaging coupled with three-dimensional (3D) cell surface rendering revealed that microglia in *Nlrp3*^{D301N}-cKI mice contained comparable to fewer numbers of PSD-95$^+$ puncta compared with microglia from control mice (Figures S4A–S4E). We also examined synaptic engulfment using a viral reporter that expresses PSD-95-mCherry-EGFP or gephyrin-mCherry-EGFP.[26] Whereas both mCherry and EGFP exhibit consistent fluorescence at neutral pH, only mCherry$^+$ signals remain intact in acidic lysosomal compartments, enabling the demonstration of microglial engulfment of PSD-95- or gephyrin-containing post-synapses (Figures S4F and S4G). The numbers of mCherry$^+$ EGFP$^-$ puncta in both PSD-95- and gephyrin-containing postsynapses within microglia were comparable between control and *Nlrp3*^{D301N}-cKI mice (Figures S4H and S4I). Taken together, these results indicate that the specific loss of excitatory postsynaptic compartments observed in LPS-treated *Nlrp3*^{D301N}-cKI mice is not likely caused by microglia-mediated synapse engulfment.

Anxiety-like and repetitive behaviors are induced by excessive NLRP3-mediated neuroinflammation

Next, to investigate the effect of *Nlrp3*^{D301N}-cKI-mediated inflammation on cognitive functions, we performed a battery of behavioral assays (Figures 2A and S5A). It was reported that systemic administration of LPS produces a spectrum of acute behavioral responses termed sickness behavior, resulting in body weight loss and reduced locomotor activity.[27] We previously showed that the significant loss of body weight and reduction in locomotor activity induced by LPS injection were recovered to ∼90% of controls 4 days after LPS injections.[28] Here, we found that the locomotor activity of LPS-injected *Nlrp3*^{D301N}-cKI mice also recovered to approximately normal at

CellPress
OPEN ACCESS

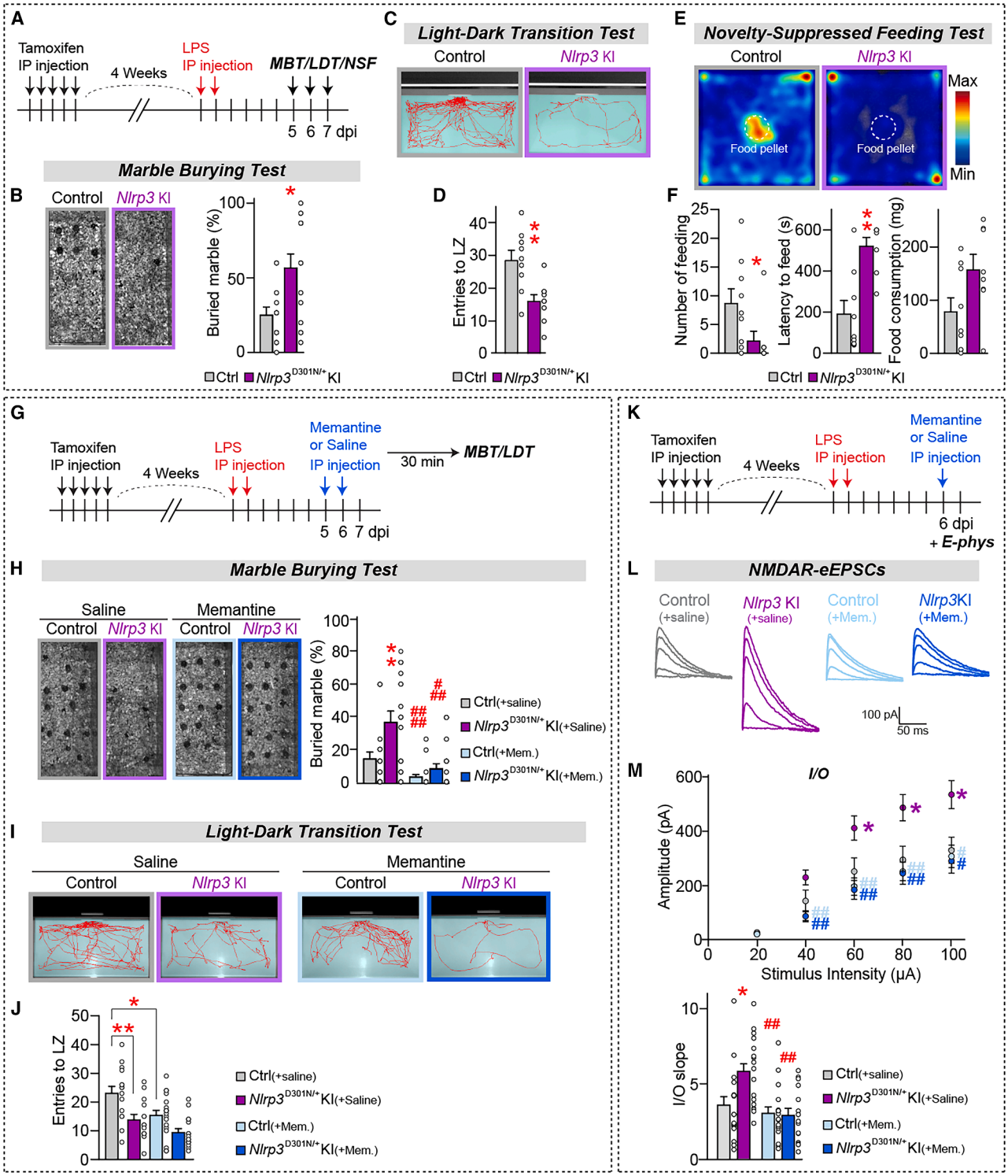

Figure 2. *Nlrp3*^{D301N}-cKI mice exhibit increased anxiety and repetitive behaviors, which can be selectively ameliorated by memantine treatment

(A) Schematic illustration of the experimental procedure.

(B) Representative photographs from the MBT and a summary graph showing the percentage of buried marbles.

(C) Representative track images during the LDT test.

(D) The number of entries into the light zone (LZ) is shown.

(legend continued on next page)

4 dpi, but the body weight of these mice was not fully restored until 6 dpi (Figures S5B–S5E). In addition, *Nlrp3*^{D301N}-cKI mice exhibited normal social interaction and social novelty-recognition memory, as assessed by the three-chamber test (Figures S5F–S5I), and displayed comparable ultrasonic vocalization calls (Figures S5J and S5K). Interestingly, however, *Nlrp3*^{D301N}-cKI mice displayed increased repetitive behavior, as assessed by counting buried marbles in a marble burying test (MBT) (Figure 2B). In addition, in the light-dark transition (LDT) test, which assesses anxiety in response to bright light, *Nlrp3*^{D301N}-cKI mice exhibited a significantly reduced number of entries into the brightly lit chamber (Figures 2C and 2D), suggesting that excessive NLRP3-mediated inflammation increases bright-light-induced anxiety. To confirm that *Nlrp3*^{D301N}-cKI mice are more vulnerable to anxiety, we additionally performed a novelty-suppressed feeding (NSF) test. *Nlrp3*^{D301N}-cKI mice showed a dramatic increase in latency to feed and a decreased frequency of feeding in the NSF test (Figures 2E and 2F), confirming increased anxiety in these mice. Taken together, these results suggest that NLRP3-mediated excessive neuroinflammation leads to increased repetitive and anxiety behaviors.

Suppressing NMDAR hyperactivation reverses increased repetitive behavior induced by NLRP3-mediated neuroinflammation

Next, we designed pharmacological rescue experiments to link the consequences of enhanced NMDAR functions with behavioral deficits observed in *Nlrp3*^{D301N}-cKI mice. Acute treatment with the NMDAR antagonist memantine (10 mg/kg body weight; intraperitoneal [i.p.]) into *Nlrp3*^{D301N}-cKI mice normalized the repetitive behaviors observed in *Nlrp3*^{D301N}-cKI mice (Figures 2G and 2H). However, memantine treatment did not restore anxiety-like behaviors to levels comparable to those of control mice, as measured by LDT tests (Figures 2I and 2J). Administration of a single acute dose of memantine also normalized the elevated NMDAR-mediated eEPSCs in *Nlrp3*^{D301N}-cKI mice (Figures 2K–2M).

To determine whether memantine-induced improvement in behavioral performance was correlated with the reversal of excitatory synaptic deficits found in *Nlrp3*^{D301N}-cKI mice, we performed an immunofluorescence analysis using anti-PSD-95 antibodies. Intriguingly, acute memantine treatment did not rescue the reduced density of PSD-95^{+} puncta in the mPFC of adult *Nlrp3*^{D301N}-cKI mice (Figures S5L–S5O). In addition, memantine treatment did not affect microglial activation in *Nlrp3*^{D301N}-cKI mice (Figures S5P–S5R), indicating that the microglial activation and subsequent reduction in excitatory postsynaptic number occurred before NMDAR activation during neuroinflammation. Taken together, these results suggest that the suppression of NMDAR hyperactivation could reverse deficits in repetitive, but not anxiety-like, behaviors after or during excessive neuroinflammation.

IL-1β drives abnormal NMDAR function in cultured cortical neurons in association with altered levels of surface GluN2A subunit-containing NMDARs

To unravel the molecular mechanisms by which excessive *Nlrp3*^{D301N}-cKI-triggered inflammation alters excitatory synapse number and NMDAR function, we first utilized contactless microglia-neuron co-cultures in a Transwell system. In this approach, the neuronal medium is conditioned by factors released from activated *Nlrp3*^{D301N}-cKI microglia without direct cell-to-cell interactions between microglia and neurons. Primary microglial cells from control or *Nlrp3*^{D301N}-cKI mice on Transwells were activated by exposure to LPS for 3 h and positioned on top of a 13 days *in vitro* (DIV13) primary neuronal culture for an additional 24 h before determination of excitatory synaptic density by confocal imaging of neurons (Figure 3A). Confocal imaging analyses demonstrated that primary neurons co-cultured with LPS-treated microglia derived from *Nlrp3*^{D301N}-cKI mice using a Transwell system exhibited significantly decreased numbers of puncta for the excitatory postsynaptic marker SHANK (Figures 3B and 3C), similar to phenotypes observed in LPS-treated *Nlrp3*^{D301N}-cKI mice. Intriguingly, surface levels of GluN2A^{+} NMDARs, but not GluN2B^{+} NMDARs, were significantly increased in neurons co-cultured with LPS-treated microglia derived from *Nlrp3*^{D301N}-cKI mice (Figures 3B and 3C). These data suggest that the secretory activity of activated *Nlrp3*^{D301N}-cKI microglia leads to a decrease in excitatory postsynaptic number and an increase in the surface levels of GluN2A subunit-containing NMDARs.

Analyses of cerebral brain lysates using cytokine arrays showed that LPS induced a dramatic increase in various pro-inflammatory cytokines, including IL-1β, in *Nlrp3*^{D301N}-cKI mice compared with control mice at 1 dpi (Figure 3D). RT-qPCR analyses also showed that mRNA levels of several pro-inflammatory cytokine genes, including IL-1β and TNF-α, were elevated in *Nlrp3*^{D301N}-cKI mice at 1 dpi (Figure 3E). At 6 dpi, the pro-inflammatory cytokine levels remained significantly higher in *Nlrp3*^{D301N}-cKI mice compared with control mice, although to a lesser degree than seen at 1 dpi (Figure 3F). Consistent with these results, enzyme-linked immunosorbent assays (ELISAs) revealed that the concentrations of IL-1β were significantly increased in cerebral regions of *Nlrp3*^{D301N}-cKI mice at 1 dpi, and these trends persisted at 6 dpi (Figures 3G and 3H). Then, we monitored the effects of IL-1β on excitatory synaptic structure and function in cultured cortical neurons. IL-1β treatment

(E) Representative heatmaps during the NSF test.
(F) Number of feedings (left), latency to feed (middle), and the amount of food consumed in the home cage (right) are shown.
(G) Schematic illustration of the experimental procedure.
(H) Representative photographs from the MBT and a summary graph showing the percentage of buried marbles.
(I) Representative track images during the LDT test.
(J) The number of entries into the LZ is shown.
(K) Schematic illustration of the experimental procedure.
(L) Representative NMDAR-eEPSC traces.
(M) Summary plots of the NMDAR-eEPSC amplitudes as a function of stimulation current and a summary graph of fitted linear I-O slopes.

CellPress
OPEN ACCESS

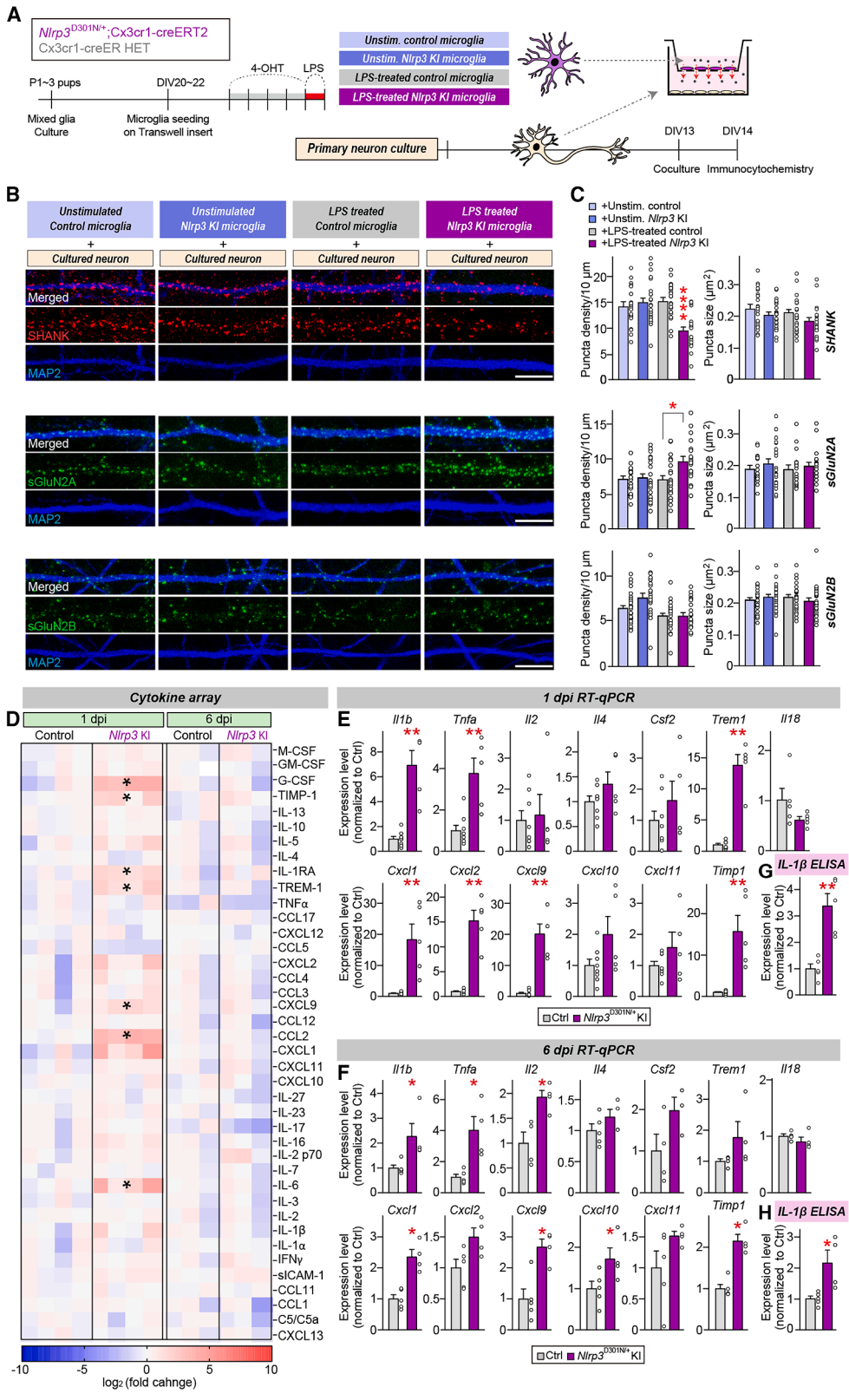

(legend on next page)

for 24 h significantly decreased the excitatory postsynaptic number and increased the surface levels of GluN2A (Figures 4A and 4B). Surface biotinylation assays revealed that IL-1β treatment selectively increased the surface levels of GluN2A but not those of GluN1 or GluN2B (Figures 4C and 4D). This led us to ask how IL-1β specifically regulates GluN2A surface levels. Previous reports showed that IL-1 receptors (IL-1Rs) form complexes with NMDARs.[29,30] Consistently, our coimmunoprecipitation assays using adult mouse brain synaptosomal fractions confirmed that IL-1Rs form complexes with NMDARs *in vivo*. Interestingly, we found that IL-1Rs preferentially form complexes with GluN2A-containing rather than GluN2B-containing NMDARs (Figures 4E and 4F). These findings suggest that the IL-1β-mediated activation of IL-1Rs might specifically facilitate GluN2A surface expression.

Electrophysiological analyses revealed that IL-1β treatment of cultured neurons increased the amplitudes of NMDAR-eEPSCs without altering those of AMPAR-eEPSCs (Figures 4G, 4H, S6C, and S6D) but decreased the frequency of mEPSCs (Figures S6A and S6B). The latter observation was in line with the reduced numbers of excitatory synapses found in neurons co-cultured with LPS-treated *Nlrp3*^{D301N}-cKI microglia (Figures 3B and 3C). When we recorded postsynaptic currents following direct applications of exogenous AMPA (1 μM) or NMDA (10 μM) (i.e., puffing experiments), IL-1β-treated neurons exhibited significantly increased peak amplitudes of NMDAR-mediated postsynaptic currents and total charge transfer but no change in the peak amplitudes of AMPAR-mediated postsynaptic currents (Figures 4I, 4J, S6E, and S6F). Taken together, these results suggest that IL-1β released from activated *Nlrp3*^{D301N}-cKI microglia is responsible for NLRP3 inflammasome-mediated effects on excitatory postsynaptic numbers and NMDAR function.

IL-1R blockade reverses the abnormal repetitive behaviors induced by excessive NLRP3-mediated neuroinflammation via normalization of NMDAR functions

To investigate whether IL-1β released from activated *Nlrp3*^{D301N}-cKI microglia mediates the behavioral deficits observed in *Nlrp3*^{D301N}-cKI mice, we performed MBT and LDT tests using control and *Nlrp3*^{D301N}-cKI mice treated with an IL-1R antagonist (IL-1RA) (Figure 4K). Acute administration of IL-1RA into *Nlrp3*^{D301N}-cKI mice reversed the abnormal repetitive behaviors but failed to rescue the anxiety-like behaviors observed in these mice (Figures 4L–4O). In addition, acute treatment of IL-1RA normalized the enhanced NMDAR-eEPSCs in mPFC regions of *Nlrp3*^{D301N}-cKI mice (Figures 4P and 4Q). These results suggest that IL-1β could be a key mediator of abnormal NMDAR activation in the excessive NLRP3-mediated neuroinflammation, leading to abnormal repetitive behaviors in mice.

DISCUSSION

Traditionally, research on brain disorders has primarily focused on understanding underlying pathophysiological mechanisms from a neuron-centric viewpoint. Recently, however, attention has shifted toward understanding the role of neuroinflammation as a driver of brain disorders ranging from schizophrenia and depression to AD.[31–34] Although previous studies using *Nlrp3*-KO mice have been reported that NLRP3-mediated neuroinflammation is associated with alterations in neuronal or cognitive functions, such as fear memory and depression-like behaviors,[14,35,36] these findings were based on systemic deletion of NLRP3. In the present study, by contrast, we utilized microglia-specific *Nlrp3*^{D301N}-cKI mice in which the activation of the NLRP3 inflammasome in microglia is likely to be long lasting and plays roles in alterations of synaptic and circuit properties of neurons. Moreover, in the present work, we performed extensive imaging, electrophysiological recordings, and behavioral analyses to understand the impact of neuroinflammation on synaptic properties and cognitive function, gaining insight into the mechanistic underpinnings of microglia-neuron interactions.

We found that NLRP3-mediated neuroinflammation and subsequent microglial activation eventually impaired excitatory synaptic functions, namely reducing excitatory postsynaptic puncta density and increasing NMDAR responses. Although these two phenotypes might appear to be paradoxical, it is possible that compensatory homeostatic mechanisms could make up for the loss of excitatory postsynaptic structures by increasing excitatory synaptic inputs. Microglia are crucial for synapse pruning, a process vital for sculpting neural circuits during the development as well as maintenance of synaptic homeostasis in the mature brain.[25,37] During this process, microglia engage in the direct removal of synaptic elements through microglial phagocytosis triggered by a classical complement cascade.[37–39] In addition, microglia modulate synapse formation and elimination by releasing cytokines, ultimately influencing neurons through the binding of cytokines to their cognate receptors and initiation of signaling cascades that control the activity and stability of synapses.[40] In the current study, we found that LPS administration in microglia-specific *Nlrp3*^{D301N}-cKI mice did not alter the engulfment of PSD-95-containing postsynaptic structures. Additionally, LPS-stimulated primary microglia from *Nlrp3*^{D301N}-cKI mice altered excitatory synaptic structures; this occurred without direct contact, suggesting that these alterations may be driven by pro-inflammatory cytokines released from microglia. In support of this notion, IL-1β treatment recapitulated the reduced excitatory postsynaptic density, increased NMDAR function, and elevated GluN2A levels in cultured neurons. IL-1β binds to and activates its cognate receptor, IL-1R1, leading to downstream signaling activation in neurons.[41] In addition, IL-1β affects the density and morphology of

Figure 3. *Nlrp3*^{D301N}-cKI microglia co-culture increases surface GluN2A levels in cultured neurons

(A) Schematic illustration of the experimental procedure. 4-OHT, 4-hydroxytamoxifen.

(B) Representative images of cultured cortical neurons immunostained with antibodies against SHANK, surface GluN2A, surface GluN2B, and MAP2.

(C) Summary graphs of puncta density and size for the indicated markers.

(D) Heatmap of cytokines levels in the brains of *Nlrp3*^{D301N}-cKI mice 1 or 6 days after LPS administration, normalized to mean levels in the control mice.

(E and F) RT-qPCR analysis of the indicated cytokines in cortices collected from control or *Nlrp3*^{D301N}-cKI mice 1 (E) or 6 (F) days after LPS administration.

(G and H) Measurement of IL-1β levels by ELISA from whole-brain tissue lysates of control versus *Nlrp3*^{D301N}-cKI mice 1 (G) or 6 (H) days after LPS treatment.

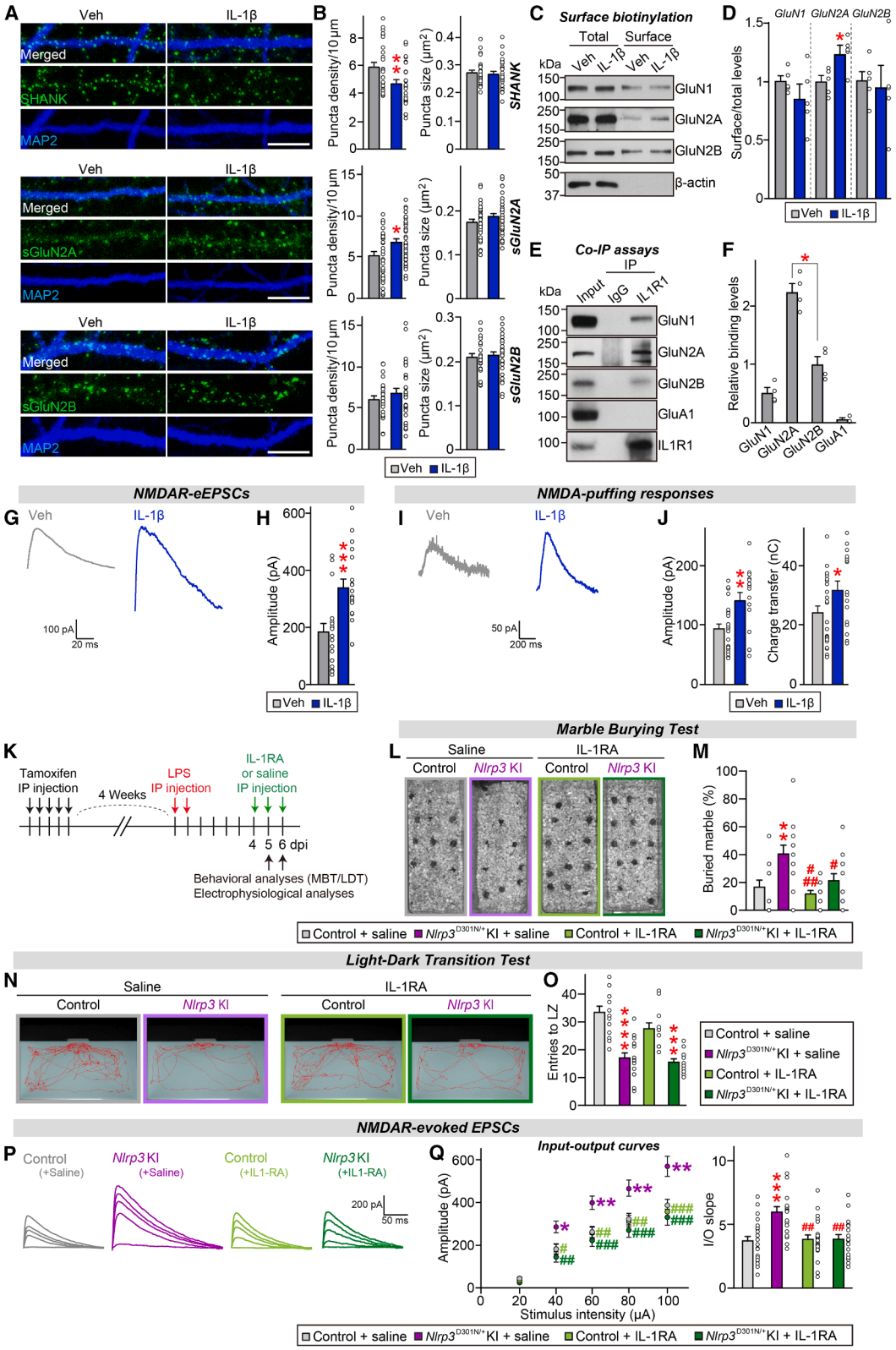

(legend on next page)

excitatory synapses and facilitates the activation of NMDAR through that of Src to increase excitotoxicity.[30,41–43] The effects of IL-1β on excitatory synaptic transmission can vary depending on the experimental conditions. Contrary to our results, IL-1β treatment was previously reported to increase excitatory synaptic transmission in striatal neurons.[44] However, the previous study used a higher concentration of IL-1β (30 ng/mL) and an acute application, whereas we herein exposed cultured hippocampal neurons to 1 ng/mL of IL-1β for 24 h before performing whole-cell recordings. Thus, the biological effects mediated by IL-1β may be variable and complex. A recent study showed that deletion of IL-1R1 in mice induces autism-like behaviors, accompanied by increased excitatory synaptic density, suggesting that finely tuned IL-1β levels are required to maintain proper brain functions.[42] Further studies are required to elucidate how the activation of specific cytokine receptor signaling, particularly IL-1β-mediated signaling, specifically regulates NMDAR function and how this microglia-neuron interaction contributes to shaping homeostatic upscaling of synaptic responses. Here, we found that neuroinflammation driven by dysregulated NLRP3 activation led to astrogliosis in the mPFC. This could potentially exacerbate inflammatory damage by altering astrocyte morphology and molecular profiles to promote the release of pro-inflammatory molecules.[45,46] These findings underscore the role of microglia as key regulators of neuroinflammation and show that they orchestrate astrocytic responses in this process. Further investigations are needed to fully delineate the contribution of astrogliosis to NLRP3-mediated neuroinflammation.

Excessive neuroinflammation in microglia-specific *Nlrp3*^{D301N}-cKI mice induced altered repetitive and anxiety-like behaviors, as assessed by marble burying and LDT/NSF tests, respectively. Increased marble-burying behavior is often interpreted as an indicator of compulsive tendencies rather than heightened anxiety states in rodents.[47] Moreover, the diagnostic criteria for autism spectrum disorders (ASDs) and obsessive-compulsive disorders (OCDs) encompass various manifestations of restricted or repetitive behaviors.[48] Successful memantine-based pharmacological rescue of repetitive, but not anxiety-like, behaviors of microglia-specific *Nlrp3*^{D301N}-cKI mice suggests that abnormally heightened NMDAR functions likely underlie altered synaptic and circuit properties in a subset of brain areas involved in repetitive behaviors in mice and potentially involved in pathophysiological mechanisms of ASDs and OCDs. Dysregulation of NMDARs has been consistently implicated in various neurological and neuropsychiatric disorders, including AD, schizophrenia, ASDs, depression, and epilepsy.[49–51] Thus, designing and targeting biomarkers that modulate NMDAR function, such as the negative and positive allosteric modulators (NAMs and PAMs, respectively), is a strategy that has been applied in numerous preclinical and clinical trials to alleviate symptoms of neurological and neuropsychiatric disorders.[52] In our study, memantine treatment failed to reverse the cellular abnormalities observed in *Nlrp3*^{D301N}-cKI mice, such as microglial activation and reduced excitatory postsynaptic density, but completely rescued the repetitive behavioral deficits. These results suggest that, after structural abnormalities are reduced by a given intervention, NMDAR function should be examined, as its over-activation could be a key event in triggering repetitive behaviors. Intriguingly, the administration of memantine did not alleviate anxiety-like behaviors in *Nlrp3*^{D301N}-cKI mice. This, along with our observation that memantine induced anxiety-like behaviors in control mice, implies that memantine itself may contribute to increased anxiety and/or that distinct mechanisms underlie anxiety-like behaviors in mice. Consistent with this interpretation, previous studies found that memantine treatment increases anxiety levels in rodents.[53] Future investigations are needed to completely address this conundrum.

Given that neuroinflammation contributes to the initiation and progression of most, if not all, neurological disorders, combinatorial therapeutic approaches for targeting the NLRP3 inflammasome and related signaling cascades, together with normalizing NMDAR function, might be effective in treating stratified symptoms of neurological diseases associated with neuroinflammation. Notably, the surface levels of GluN2A-containing NMDARs, but not GluN2B-containing NMDARs, were increased upon LPS stimulation of neurons co-cultured with primary *Nlrp3*^{D301N}-cKI microglia or upon IL-1β treatment of neurons. Considering that the GluN2A/GluN2B ratio is strongly associated with proper synaptic maturation and plasticity through modification of the threshold for induction of long-term potentiation[54,55] and the plausible link between increased GluN2A levels and several neurological disorders, the development of drugs to treat underlying altered behaviors associated with NLRP3-mediated chronic neuroinflammation

Figure 4. In LPS-stimulated *Nlrp3*^{D301N}-cKI mice, increased IL-1β levels mediate abnormal repetitive behaviors

(A) Representative images of cultured cortical neurons immunostained with antibodies against SHANK, surface GluN2A, surface GluN2B, and MAP2.

(B) Summary graphs of puncta density and size for the indicated markers.

(C) Representative immunoblot images for surface biotinylation assays probing the surface expression of NMDAR subunits on cultured neurons treated with vehicle or IL-1β (1 ng/ml) for 24 hr.

(D) Quantification of surface and total levels of the indicated NMDA subunits.

(E) Crude synaptosomal fractions of adult mouse brains were immunoprecipitated (IPed) with anti-IL1R1 antibody and immunoblotted with the indicated antibodies. Equal amounts of mouse immunoglobulin G (IgG) were used as a negative control. Input, 3%.

(F) Quantified relative binding levels for the indicated NMDA subunits with IL-1R, calculated as the ratios of IPed band intensities to input levels. The binding level of GluN2B was set to 1 as a reference.

(G and H) Representative traces (G) and summary graphs (H) of the NMDAR-eEPSCs measured from the cultured neurons treated with vehicle or IL-1β.

(I and J) Representative traces (I) and summary graphs (J) showing amplitudes of currents recorded in cultured neurons treated with vehicle or IL-1β following puffing application of NMDA.

(K) Schematic illustration of the experimental procedure.

(L and M) Representative from the marble-burying test (L) and a summary graph (M) showing the percentage of buried marbles.

(N and O) Representative track images (N) during the LDT test, and the number of entries into the light zone (LZ) (O).

(P) Representative NMDAR-eEPSC traces.

(Q) Summary plots of the NMDAR-eEPSC amplitudes and fitted linear I-O slopes.

would benefit from efforts to apply a subunit-specific allosteric design. Moreover, given that memantine is an FDA-approved drug for the treatment of AD, several medications targeting IL-1β are available or under development, and IL-1β inhibitory monoclonal antibodies or IL-1RA (anakinra) have been approved for inflammatory diseases, such as rheumatoid arthritis,[56] these therapeutic agents could be repurposed to alleviate inflammation-induced repetitive behaviors. In summary, the current study unambiguously demonstrated that NLRP3-mediated excessive neuroinflammation causes repetitive behaviors in mice through IL-1β-induced NMDAR hyperactivation.

Limitations of the study

This study presents several caveats that warrant consideration. First, although we used *Nlrp3*^{D301N}-floxed mice crossed with *Cx3cr1*-CreERT mice and allowed a 28-day period after tamoxifen injections for peripheral monocyte replenishment, we were unable to rule out the potential influence of peripheral immune cells that may have infiltrated into the brain parenchyma in response to LPS stimulation. Second, we observed apparent inconsistencies between structural and functional synaptic parameters in *Nlrp3*^{D301N}-cKI mice. The results obtained from measuring mEPSCs, AMPAR-eEPSCs, and excitatory synaptic numbers in *Nlrp3*^{D301N}-cKI mice appear to be discordant when viewed from a traditional synaptic neuroscience perspective. We speculate that the complicated effects of neuroinflammation might manifest as unpredictable phenotypes in various aspects of synaptic processes. Moreover, neuroinflammatory processes can independently influence structural and functional aspects of synapses through distinct molecular pathways, potentially leading to these seemingly inconsistent observations. Third, our study was unable to identify the specific causal mechanisms underlying the anxiety-like behaviors of adult male *Nlrp3*^{D301N}-cKI mice, although we showed that IL-1β-induced NMDAR hyperactivation mediates abnormal repetitive behaviors in these mice. Considering that *Nlrp3*^{D301N}-cKI microglia release multifarious factors, further investigation is needed to precisely determine which specific factors and signaling pathways are responsible for mediating these anxiety-like behaviors.

RESOURCE AVAILABILITY

Lead contact

Further information and requests for materials and data should be directed to and will be fulfilled by the lead contact, Ji Won Um (jiwonum@dgist.ac.kr).

Materials availability

This study did not generate any new materials.

Data and code availability

This study does not report original code. Any additional information required to reanalyze the data reported in this paper is available from the lead contact upon request.

ACKNOWLEDGMENTS

This study was supported by grants from the National Research Foundation of Korea (NRF) funded by the Ministry of Science and Future Planning (RS-2023-00207834 to J.-W.Y. and J.W.U. and RS-2022-NR067821 and RS-2023-NR176948 to J.W.U.) and the National Creative Research Initiative Program of the Ministry of Science and ICT (RS-2022-NR070708 to J.K.). We thank Jinha Kim (DGIST) for technical assistance.

AUTHOR CONTRIBUTIONS

J.W.U. conceived and directed the project; H.J., B.K., G.J., H.K., S.-H.Y., K.-S. L., G.H., Y.K., and J.-W.Y. performed the experiments and analyzed the results; A.-R.L. provided recombinant proteins; J.K. and J.W.U. supervised the project; and H.J., J.K., J.-W.Y., and J.W.U. wrote the paper.

DECLARATION OF INTERESTS

The authors declare no competing interests.

STAR★METHODS

Detailed methods are provided in the online version of this paper and include the following:

- KEY RESOURCES TABLE
- EXPERIMENTAL MODEL AND STUDY PARTICIPANT DETAILS
  - Animals
  - Primary microglia culture
  - Microglia-neuron co-culture using transwell
  - Culture, immunostaining, and image analysis of cultured neurons
- METHOD DETAILS
  - Drug administration
  - Immunohistochemistry
  - Analysis of microglia morphology
  - TUNEL staining
  - Preparation of brain lysates and quantification of cytokine expression level
  - Immunoblot analysis
  - Quantitative reverse transcription polymerase chain reaction (RT-qPCR)
  - Preparation and titration of AAVs
  - Stereotaxic injections
  - Behavioral analysis
  - Cloning of IL-1β and IL-1RA for expression in *E. coli*
  - Purification of IL-1β and IL-1RA
  - Coimmunoprecipitation assays
  - Biotinylation assays
  - Flow cytometry
  - *Ex vivo* electrophysiological recordings
  - *In vitro* electrophysiological recordings from cultured neurons
- QUANTIFICATION AND STATISTICAL ANALYSIS
  - Quantification of 3D microglial engulfment
  - Analysis of microglial engulfment using a synapse engulfment reporter virus
  - Statistical analysis

SUPPLEMENTAL INFORMATION

Supplemental information can be found online at https://doi.org/10.1016/j.celrep.2025.115656.

Received: September 9, 2024
Revised: February 21, 2025
Accepted: April 15, 2025
Published: May 6, 2025

REFERENCES

1. Degan, D., Ornello, R., Tiseo, C., Carolei, A., Sacco, S., and Pistoia, F. (2018). The Role of Inflammation in Neurological Disorders. Curr. Pharm. Des. *24*, 1485–1501. https://doi.org/10.2174/1381612824666180327170632.

2. Skaper, S.D., Facci, L., Zusso, M., and Giusti, P. (2018). An Inflammation-Centric View of Neurological Disease: Beyond the Neuron. Front. Cell. Neurosci. *12*, 72. https://doi.org/10.3389/fncel.2018.00072.

3. Iakunchykova, O., Leonardsen, E.H., and Wang, Y. (2024). Genetic evidence for causal effects of immune dysfunction in psychiatric disorders: where are we? Transl. Psychiatry *14*, 63. https://doi.org/10.1038/s41398-024-02778-2.

4. Bennett, F.C., and Molofsky, A.V. (2019). The immune system and psychiatric disease: a basic science perspective. Clin. Exp. Immunol. *197*, 294–307. https://doi.org/10.1111/cei.13334.

5. Felger, J.C. (2018). Imaging the Role of Inflammation in Mood and Anxiety-related Disorders. Curr. Neuropharmacol. *16*, 533–558. https://doi.org/10.2174/1570159x15666171123201142.

6. Lee, D.H., Lee, J.Y., Hong, D.Y., Lee, E.C., Park, S.W., Lee, M.R., and Oh, J.S. (2022). Neuroinflammation in Post-Traumatic Stress Disorder. Biomedicines *10*, 953. https://doi.org/10.3390/biomedicines10050953.

7. Piva, S., Bertoni, M., Gitti, N., Rasulo, F.A., and Latronico, N. (2023). Neurological complications of sepsis. Curr. Opin. Crit. Care *29*, 75–84. https://doi.org/10.1097/mcc.0000000000001022.

8. Hodes, G.E., Pfau, M.L., Leboeuf, M., Golden, S.A., Christoffel, D.J., Bregman, D., Rebusi, N., Heshmati, M., Aleyasin, H., Warren, B.L., et al. (2014). Individual differences in the peripheral immune system promote resilience versus susceptibility to social stress. Proc. Natl. Acad. Sci. USA *111*, 16136–16141. https://doi.org/10.1073/pnas.1415191111.

9. Passos, I.C., Vasconcelos-Moreno, M.P., Costa, L.G., Kunz, M., Brietzke, E., Quevedo, J., Salum, G., Magalhães, P.V., Kapczinski, F., and Kauer-Sant'Anna, M. (2015). Inflammatory markers in post-traumatic stress disorder: a systematic review, meta-analysis, and meta-regression. Lancet Psychiatry *2*, 1002–1012. https://doi.org/10.1016/s2215-0366(15)00309-0.

10. Halle, A., Hornung, V., Petzold, G.C., Stewart, C.R., Monks, B.G., Reinheckel, T., Fitzgerald, K.A., Latz, E., Moore, K.J., and Golenbock, D.T. (2008). The NALP3 inflammasome is involved in the innate immune response to amyloid-β. Nat. Immunol. *9*, 857–865. https://doi.org/10.1038/ni.1636.

11. Heneka, M.T., Kummer, M.P., Stutz, A., Delekate, A., Schwartz, S., Vieira-Saecker, A., Griep, A., Axt, D., Remus, A., Tzeng, T.C., et al. (2013). NLRP3 is activated in Alzheimer's disease and contributes to pathology in APP/PS1 mice. Nature *493*, 674–678. https://doi.org/10.1038/nature11729.

12. Tan, E.-K., Chao, Y.-X., West, A., Chan, L.-L., Poewe, W., and Jankovic, J. (2020). Parkinson disease and the immune system — associations, mechanisms and therapeutics. Nat. Rev. Neurol. *16*, 303–318. https://doi.org/10.1038/s41582-020-0344-4.

13. Kouba, B.R., Gil-Mohapel, J., and AL, S.R. (2022). NLRP3 Inflammasome: From Pathophysiology to Therapeutic Target in Major Depressive Disorder. Int. J. Mol. Sci. *24*, 133. https://doi.org/10.3390/ijms24010133.

14. Li, S., Fang, Y., Zhang, Y., Song, M., Zhang, X., Ding, X., Yao, H., Chen, M., Sun, Y., Ding, J., et al. (2022). Microglial NLRP3 inflammasome activates neurotoxic astrocytes in depression-like mice. Cell Rep. *41*, 111532. https://doi.org/10.1016/j.celrep.2022.111532.

15. Smith, C., Trageser, K.J., Wu, H., Herman, F.J., Iqbal, U.H., Sebastian-Valverde, M., Frolinger, T., Zeng, E., and Pasinetti, G.M. (2021). Anxiolytic effects of NLRP3 inflammasome inhibition in a model of chronic sleep deprivation. Transl. Psychiatry *11*, 52. https://doi.org/10.1038/s41398-020-01189-3.

16. Jo, E.-K., Kim, J.K., Shin, D.-M., and Sasakawa, C. (2016). Molecular mechanisms regulating NLRP3 inflammasome activation. Cell. Mol. Immunol. *13*, 148–159. https://doi.org/10.1038/cmi.2015.95.

17. Jones, M.E., Lebonville, C.L., Barrus, D., and Lysle, D.T. (2015). The role of brain interleukin-1 in stress-enhanced fear learning. Neuropsychopharmacology *40*, 1289–1296. https://doi.org/10.1038/npp.2014.317.

18. Vezzani, A., and Viviani, B. (2015). Neuromodulatory properties of inflammatory cytokines and their impact on neuronal excitability. Neuropharmacology *96*, 70–82. https://doi.org/10.1016/j.neuropharm.2014.10.027.

19. Dong, Y., Li, S., Lu, Y., Li, X., Liao, Y., Peng, Z., Li, Y., Hou, L., Yuan, Z., and Cheng, J. (2020). Stress-induced NLRP3 inflammasome activation negatively regulates fear memory in mice. J. Neuroinflammation *17*, 205. https://doi.org/10.1186/s12974-020-01842-0.

20. Lee, E., Hwang, I., Park, S., Hong, S., Hwang, B., Cho, Y., Son, J., and Yu, J.W. (2019). MPTP-driven NLRP3 inflammasome activation in microglia plays a central role in dopaminergic neurodegeneration. Cell Death Differ. *26*, 213–228. https://doi.org/10.1038/s41418-018-0124-5.

21. Bonar, S.L., Brydges, S.D., Mueller, J.L., McGeough, M.D., Pena, C., Chen, D., Grimston, S.K., Hickman-Brecks, C.L., Ravindran, S., McAlinden, A., et al. (2012). Constitutively activated NLRP3 inflammasome causes inflammation and abnormal skeletal development in mice. PLoS One *7*, e35979. https://doi.org/10.1371/journal.pone.0035979.

22. Ma, J.H., Lee, E., Yoon, S.H., Min, H., Oh, J.H., Hwang, I., Sung, Y., Ryu, J. H., Bok, J., and Yu, J.W. (2022). Therapeutic effect of NLRP3 inhibition on hearing loss induced by systemic inflammation in a CAPS-associated mouse model. EBioMedicine *82*, 104184. https://doi.org/10.1016/j.ebiom.2022.104184.

23. Sharif, H., Wang, L., Wang, W.L., Magupalli, V.G., Andreeva, L., Qiao, Q., Hauenstein, A.V., Wu, Z., Núñez, G., Mao, Y., and Wu, H. (2019). Structural mechanism for NEK7-licensed activation of NLRP3 inflammasome. Nature *570*, 338–343. https://doi.org/10.1038/s41586-019-1295-z.

24. Park, D., Kim, S., Kim, H., Shin, J., Jung, H., and Um, J.W. (2020). Seizure progression triggered by IQSEC3 loss is mitigated by reducing activated microglia in mice. Glia *68*, 2661–2673. https://doi.org/10.1002/glia.23876.

25. Hong, S., and Stevens, B. (2016). Microglia: Phagocytosing to Clear, Sculpt, and Eliminate. Dev. Cell *38*, 126–128. https://doi.org/10.1016/j.devcel.2016.07.006.

26. Lee, J.H., Kim, J.Y., Noh, S., Lee, H., Lee, S.Y., Mun, J.Y., Park, H., and Chung, W.S. (2021). Astrocytes phagocytose adult hippocampal synapses for circuit homeostasis. Nature *590*, 612–617. https://doi.org/10.1038/s41586-020-03060-3.

27. Kent, S., Bluthé, R.M., Kelley, K.W., and Dantzer, R. (1992). Sickness behavior as a new target for drug development. Trends Pharmacol. Sci. *13*, 24–28. https://doi.org/10.1016/0165-6147(92)90012-u.

28. Jung, H., Lee, D., You, H., Lee, M., Kim, H., Cheong, E., and Um, J.W. (2023). LPS induces microglial activation and GABAergic synaptic deficits in the hippocampus accompanied by prolonged cognitive impairment. Sci. Rep. *13*, 6547. https://doi.org/10.1038/s41598-023-32798-9.

29. Gardoni, F., Boraso, M., Zianni, E., Corsini, E., Galli, C.L., Cattabeni, F., Marinovich, M., Di Luca, M., and Viviani, B. (2011). Distribution of interleukin-1 receptor complex at the synaptic membrane driven by interleukin-1β and NMDA stimulation. J. Neuroinflammation *8*, 14. https://doi.org/10.1186/1742-2094-8-14.

30. Viviani, B., Bartesaghi, S., Gardoni, F., Vezzani, A., Behrens, M.M., Bartfai, T., Binaglia, M., Corsini, E., Di Luca, M., Galli, C.L., and Marinovich, M. (2003). Interleukin-1β Enhances NMDA Receptor-Mediated Intracellular Calcium Increase through Activation of the Src Family of Kinases. J. Neurosci. *23*, 8692–8700. https://doi.org/10.1523/jneurosci.23-25-08692.2003.

31. Leng, F., and Edison, P. (2021). Neuroinflammation and microglial activation in Alzheimer disease: where do we go from here? Nat. Rev. Neurol. *17*, 157–172. https://doi.org/10.1038/s41582-020-00435-y.

32. Müller, N., Weidinger, E., Leitner, B., and Schwarz, M.J. (2015). The role of inflammation in schizophrenia. Front. Neurosci. *9*, 372. https://doi.org/10.3389/fnins.2015.00372.

33. Monji, A., Kato, T.A., Mizoguchi, Y., Horikawa, H., Seki, Y., Kasai, M., Yamauchi, Y., Yamada, S., and Kanba, S. (2013). Neuroinflammation in schizophrenia especially focused on the role of microglia. Prog.

Neuropsychopharmacol. Biol. Psychiatry *42*, 115–121. https://doi.org/10.1016/j.pnpbp.2011.12.002.

34. Richardson, B., MacPherson, A., and Bambico, F. (2022). Neuroinflammation and neuroprogression in depression: Effects of alternative drug treatments. Brain Behav. Immun. Health *26*, 100554. https://doi.org/10.1016/j.bbih.2022.100554.
35. Beyer, M.M.S., Lonnemann, N., Remus, A., Latz, E., Heneka, M.T., and Korte, M. (2020). Enduring Changes in Neuronal Function upon Systemic Inflammation Are NLRP3 Inflammasome Dependent. J. Neurosci. *40*, 5480–5494. https://doi.org/10.1523/jneurosci.0200-20.2020.
36. Komleva, Y.K., Lopatina, O.L., Gorina, I.V., Shuvaev, A.N., Chernykh, A., Potapenko, I.V., and Salmina, A.B. (2021). NLRP3 deficiency-induced hippocampal dysfunction and anxiety-like behavior in mice. Brain Res. *1752*, 147220. https://doi.org/10.1016/j.brainres.2020.147220.
37. Tremblay, M.È., Stevens, B., Sierra, A., Wake, H., Bessis, A., and Nimmerjahn, A. (2011). The role of microglia in the healthy brain. J. Neurosci. *31*, 16064–16069. https://doi.org/10.1523/jneurosci.4158-11.2011.
38. Schafer, D.P., Lehrman, E.K., Kautzman, A.G., Koyama, R., Mardinly, A.R., Yamasaki, R., Ransohoff, R.M., Greenberg, M.E., Barres, B.A., and Stevens, B. (2012). Microglia sculpt postnatal neural circuits in an activity and complement-dependent manner. Neuron *74*, 691–705. https://doi.org/10.1016/j.neuron.2012.03.026.
39. Stevens, B., Allen, N.J., Vazquez, L.E., Howell, G.R., Christopherson, K.S., Nouri, N., Micheva, K.D., Mehalow, A.K., Huberman, A.D., Stafford, B., et al. (2007). The classical complement cascade mediates CNS synapse elimination. Cell *131*, 1164–1178. https://doi.org/10.1016/j.cell.2007.10.036.
40. Werneburg, S., Feinberg, P.A., Johnson, K.M., and Schafer, D.P. (2017). A microglia-cytokine axis to modulate synaptic connectivity and function. Curr. Opin. Neurobiol. *47*, 138–145. https://doi.org/10.1016/j.conb.2017.10.002.
41. Zipp, F., Bittner, S., and Schafer, D.P. (2023). Cytokines as emerging regulators of central nervous system synapses. Immunity *56*, 914–925. https://doi.org/10.1016/j.immuni.2023.04.011.
42. Borreca, A., Mantovani, C., Desiato, G., Corradini, I., Filipello, F., Elia, C.A., D'Autilia, F., Santamaria, G., Garlanda, C., Morini, R., et al. (2024). Loss of interleukin 1 signaling causes impairment of microglia- mediated synapse elimination and autistic-like behaviour in mice. Brain Behav. Immun. *117*, 493–509. https://doi.org/10.1016/j.bbi.2024.01.221.
43. Tomasoni, R., Morini, R., Lopez-Atalaya, J.P., Corradini, I., Canzi, A., Rasile, M., Mantovani, C., Pozzi, D., Garlanda, C., Mantovani, A., et al. (2017). Lack of IL-1R8 in neurons causes hyperactivation of IL-1 receptor pathway and induces MECP2-dependent synaptic defects. Elife *6*, e21735. https://doi.org/10.7554/eLife.21735.
44. Rossi, S., Furlan, R., De Chiara, V., Motta, C., Studer, V., Mori, F., Musella, A., Bergami, A., Muzio, L., Bernardi, G., et al. (2012). Interleukin-1β causes synaptic hyperexcitability in multiple sclerosis. Ann. Neurol. *71*, 76–83. https://doi.org/10.1002/ana.22512.
45. Giovannoni, F., and Quintana, F.J. (2020). The Role of Astrocytes in CNS Inflammation. Trends Immunol. *41*, 805–819. https://doi.org/10.1016/j.it.2020.07.007.
46. Liddelow, S.A., Guttenplan, K.A., Clarke, L.E., Bennett, F.C., Bohlen, C.J., Schirmer, L., Bennett, M.L., Münch, A.E., Chung, W.S., Peterson, T.C., et al. (2017). Neurotoxic reactive astrocytes are induced by activated microglia. Nature *541*, 481–487. https://doi.org/10.1038/nature21029.
47. Thomas, A., Burant, A., Bui, N., Graham, D., Yuva-Paylor, L.A., and Paylor, R. (2009). Marble burying reflects a repetitive and perseverative behavior more than novelty-induced anxiety. Psychopharmacology (Berl) *204*, 361–373. https://doi.org/10.1007/s00213-009-1466-y.
48. O'Loghlen, J., McKenzie, M., Lang, C., and Paynter, J. (2024). Repetitive Behaviors in Autism and Obsessive-Compulsive Disorder: A Systematic Review. J. Autism Dev. Disord. *54*, 3194–3196. https://doi.org/10.1007/s10803-024-06450-y.
49. Tarabeux, J., Kebir, O., Gauthier, J., Hamdan, F.F., Xiong, L., Piton, A., Spiegelman, D., Henrion, É., Millet, B., et al.; S2D team (2011). Rare mutations in N-methyl-D-aspartate glutamate receptors in autism spectrum disorders and schizophrenia. Transl. Psychiatry *1*, e55. https://doi.org/10.1038/tp.2011.52.
50. XiangWei, W., Jiang, Y., and Yuan, H. (2018). De Novo Mutations and Rare Variants Occurring in NMDA Receptors. Curr. Opin. Physiol. *2*, 27–35. https://doi.org/10.1016/j.cophys.2017.12.013.
51. Lee, E.-J., Choi, S.Y., and Kim, E. (2015). NMDA receptor dysfunction in autism spectrum disorders. Curr. Opin. Pharmacol. *20*, 8–13. https://doi.org/10.1016/j.coph.2014.10.007.
52. Hanson, J.E., Yuan, H., Perszyk, R.E., Banke, T.G., Xing, H., Tsai, M.-C., Menniti, F.S., and Traynelis, S.F. (2024). Therapeutic potential of N-methyl-D-aspartate receptor modulators in psychiatry. Neuropsychopharmacology *49*, 51–66. https://doi.org/10.1038/s41386-023-01614-3.
53. Shuvaev, A.N., Belozor, O.S., Mozhei, O.I., Mileiko, A.G., Mosina, L.D., Laletina, I.V., Mikhailov, I.G., Fritsler, Y.V., Shuvaev, A.N., Teschemacher, A.G., and Kasparov, S. (2022). Memantine Disrupts Motor Coordination through Anxiety-like Behavior in CD1 Mice. Brain Sci. *12*, 495. https://doi.org/10.3390/brainsci12040495.
54. Shipton, O.A., and Paulsen, O. (2014). GluN2A and GluN2B subunit-containing NMDA receptors in hippocampal plasticity. Philos. Trans. R. Soc. Lond. B Biol. Sci. *369*, 20130163. https://doi.org/10.1098/rstb.2013.0163.
55. Tian, M., Stroebel, D., Piot, L., David, M., Ye, S., and Paoletti, P. (2021). GluN2A and GluN2B NMDA receptors use distinct allosteric routes. Nat. Commun. *12*, 4709. https://doi.org/10.1038/s41467-021-25058-9.
56. Dinarello, C.A. (2011). Interleukin-1 in the pathogenesis and treatment of inflammatory diseases. Blood *117*, 3720–3732. https://doi.org/10.1182/blood-2010-07-273417.
57. Kim, S., Kang, M., Park, D., Lee, A.R., Betz, H., Ko, J., Chang, I., and Um, J.W. (2021). Impaired formation of high-order gephyrin oligomers underlies gephyrin dysfunction-associated pathologies. iScience *24*, 102037. https://doi.org/10.1016/j.isci.2021.102037.

STAR★METHODS

KEY RESOURCES TABLE

REAGENT or RESOURCE	SOURCE	IDENTIFIER
Antibodies		
Rabbit polyclonal Anti-Iba-1	Fujifilm Wako	Cat# 016–20001; RRID:AB_839506
Rat monoclonal Anti-CD68	Bio-Rad	Cat# MCA1957GA; RRID:AB_324217
Goat polyclonal Anti-EGFP	Rockland	Cat# 600-101-215; RRID:AB_218182
Rabbit polyclonal Anti-VGLUT1	Jaewon Ko's lab (DGIST)	JK111; RRID:AB_2810945
Rabbit polyclonal Anti-PSD-95	Jaewon Ko's lab (DGIST)	JK016; RRID:AB_2722693
Rabbit polyclonal Anti-VGAT	Synaptic Systems	Cat# 131 003; RRID:AB_887869
Rabbit polyclonal Anti-$GABA_AR\gamma2$	Synaptic Systems	Cat# 224 003; RRID:AB_2263066
Rabbit polyclonal Anti-GFAP	Agilent	Cat# Z0334; RRID:AB_10013382
Guinea pig polyclonal Anti-S100β	Synaptic Systems	Cat# 287 004; RRID:AB_2620025
Chicken polyclonal Anti-MAP2	BioLegend	Cat# 822501; RRID:AB_2564858
Rabbit polyclonal Anti-pan-SHANK	Eunjoon Kim's lab (KAIST/IBS)	1172; RRID: AB_2810261
Rabbit polyclonal Anti-GluN2A	Alomone Labs	Cat# AGC-002, RRID:AB_2040025
Rabbit polyclonal Anti-GluN2B	Alomone Labs	Cat# AGC-003; RRID:AB_2040028
Guinea pig polyclonal Anti-VGLUT1	Millipore	Cat# AB5905; RRID:AB_2301751
Mouse monoclonal Anti-gephyrin	Synaptic Systems	Cat# 147 111; RRID:AB_887719
Rabbit polyclonal Anti-GluA1	Eunjoon Kim's lab (KAIST/IBS)	1193; RRID:AB_2722772
Mouse monoclonal Anti-GluN1	Millipore	Cat# MAB363; RRID:AB_94946
Rabbit polyclonal Anti-GluN2A	Millipore	Cat# 07–632; RRID:AB_310837
Mouse monoclonal Anti-GluN2B	Millipore	Cat# 05–920; RRID:AB_417391
Rat monoclonal Anti-CD45	Biolegend	Cat# 103116; RRID:AB_312981
Rat monoclonal Anti-CD11b	Thermo Fisher Scientific	Cat# 12-0112-82; RRID:AB_2734869
Rat monoclonal Anti-Ly6C	Thermo Fisher Scientific	Cat# 53-5932-82; RRID:AB_2574427
Rat monoclonal Anti-Ly6G	Thermo Fisher Scientific	Cat# 17-9668-82; RRID:AB_2573307
Cy3 conjugated Donkey Anti-Rabbit	Jackson ImmunoResearch Labs	Cat# 711-165-152, RRID:AB_2307443
Cy3 conjugated Donkey Anti-Rat	Jackson ImmunoResearch Labs	Cat# 712-165-153, RRID:AB_2340667
Cy3 conjugated Goat Anti-Guinea pig	Abcam	Cat# ab102370; RRID:AB_10711466
FITC conjugated Donkey Anti-Rabbit	Jackson ImmunoResearch Labs	Cat# 711-095-152, RRID:AB_2315776
FITC conjugated Donkey Anti-Goat	Jackson ImmunoResearch Labs	Cat# 705-095-147, RRID:AB_2340401
AF488 conjugated Donkey Anti-Chicken	Jackson ImmunoResearch Labs	Cat# 703-545-155, RRID:AB_2340375
AF647 conjugated Donkey Anti-Rabbit	Thermo Fisher Scientific	Cat# A-31573, RRID:AB_2536183
HRP-conjugated Affinipure Donkey anti-Rabbit IgG (H + L)	Jackson ImmunoResearch Labs	Cat# 711-035-152, RRID:AB_10015282
HRP-conjugated Affinipure Donkey anti-Mouse IgG (H + L)	Jackson ImmunoResearch Labs	Cat# 715-035-150, RRID:AB_2340770
HRP-conjugated Affinipure Donkey anti-Guinea Pig IgG (H + L)	Jackson ImmunoResearch Labs	Cat# 706-035-148, RRID:AB_2340447
Chemicals, peptides, and recombinant proteins		
Tamoxifen	Sigma	Cat#: T5648-1G
corn oil	Sigma	Cat#: C8267
Lipopolysaccharides from *E. coli* O111:B4	Sigma	Cat#: L3012
Memantine hydrochloride	Sigma	Cat#: M9292
Trypsin-EDTA	WELGENE	Cat#: LS015-10
DMEM	WELGENE	Cat#: LM001-05

(*Continued on next page*)

Continued

REAGENT or RESOURCE	SOURCE	IDENTIFIER
Fetal Bovine Serum (FBS)	WELGENE	Cat#: PK004-01
Penicillin/Streptomycin	ThermoFisher Scientific	Cat#: 15140122
PEI MAX	Polyscience	Cat#: 24765-1
Lipofectamine LTX Reagent with PLUSTM Reagent	ThermoFisher Scientific	Cat#: 15338100
HBSS (Hanks' Balanced Salt Solution)	ThermoFisher	Cat#: 14065056
Papain	Worthington	Cat#: LS003126
Neurobasal medium	ThermoFisher Scientific	Cat#: 21103049
B-27 supplement (50X)	ThermoFisher Scientific	Cat#: 17504-044
GlutaMax Supplement	ThermoFisher Scientific	Cat#: 35050061
Sodium pyruvate	ThermoFisher Scientific	Cat#: 11360070
DMEM/F-12	Cytiva	Cat#: SH30023.01
4-hydroxytamoxifen	Sigma	Cat#: H7904
Poly-D-lysine hydrobromide	Sigma	Cat#: P0899
Paraformaldehyde	Sigma	Cat#: 158127
37% formaldehyde	Biosesang	Cat#: F1012
Triton X-100	Sigma	Cat#: T8787
Bovine serum albumin	Sigma	Cat#: A7906
Horse serum	Gibco	Cat#: 16050122
Vectashield mounting medium	Vector Laboratories	Cat#: H-1200, H-1000
DNaseI	Sigma	Cat#: AMPD1
human recombinant IL-1β	This study	N/A
human recombinant IL-1RA	This study	N/A
Poly(ethylene glycol); PEG	Sigma	Cat #: P5413
Chloroform	Millipore	Cat#: 102445
TRIzol reagent	Ambicon	Cat#: BRL-15596-026
ReverTra Ace-α kit	TOYOBO	Cat#: TOFSQ-301
TB green qPCR master mix	Takara	Cat#: RR420A
DL-2-amino-5-phosphonopentanoic acid (DL-APV)	Sigma	Cat#: A5282
6-cyano-7-nitroquinoxaline-2,3-dione (CNQX)	Sigma	Cat#: C127
Picrotoxin	Tocris	Cat#: 1128
Tetrodoxin	Tocris	Cat#: 1069
Critical commercial assays		
mouse IL-1β DuoSet ELISA kit	R&D Systems	Cat#: DY401
DuoSet ELISA Ancillary Reagent Kit	R&D Systems	Cat#: DY008
Proteome Profiler Mouse Cytokine Array Kit	R&D Systems	Cat#: ARY006
In Situ Cell Death Detection Kit, TMR red	Roche	Cat#: 12156792910
Experimental models: cell lines		
HEK293T cells	ATCC	Cat#: CRL-3216
Cultured neuronal cells	N/A	N/A
Cultured microglial cells	N/A	N/A
Experimental models: organisms/strains		
Mouse: *Nlrp3*D301NneoR	The Jackson Laboratory	Cat#: 017971
Mouse: Cx3cr1-CreERT2	The Jackson Laboratory	Cat#: 021160
Rat: E18 pregnant females (Sprague-Dawley)	Daehan Biolink	N/A
Recombinant DNA		
pAAV-CW3SL:hSyn-PSD95-mCherry-eGFP (ExPost)	Lee et al.[26]	N/A
pAAV-CW3SL:hSyn-gephyrin-mCherry-eGFP (InhiPost)	Lee et al.[26]	N/A

(*Continued on next page*)

Continued

REAGENT or RESOURCE	SOURCE	IDENTIFIER
Software and algorithms		
Zen2.6	Zeiss	https://www.zeiss.com/microscopy/en/products/software/zeiss-zen.html
MetaMorph	Molecular Devices	https://www.moleculardevices.com
ImageJ	NIH	https://imagej.nih.gov/ij
Imaris	Oxford Instruments	https://imaris.oxinst.com
GraphPad Prism 8.0	GraphPad	https://www.graphpad.com
EthoVision XT 15	Noldus	http://www.noldus.com/animal-behavior-research/products/ethovision-xt
Avisoft SASLab Pro	Avisoft Bioacoustics	https://avisoft.com/sound-analysis
Mini Analysis	Synaptosoft	https://www.synaptosoft.com/MiniAnalysis
Clampfit 10.8 software	Molecular Devices	https://www.moleculardevices.com/products/axon-patch-clamp-system/acquisition-and-analysis-software/pclamp-software-suite

EXPERIMENTAL MODEL AND STUDY PARTICIPANT DETAILS

Animals

The *Nlrp3*^{D301N} (D301N mutant KI) mouse (#017971) and Cx3cr1-CreERT2 mouse (#021160) were purchased from Jackson Laboratories. Microglia-specific expression of the Nlrp3 D301N mutation was established by crossing *Nlrp3*^{D301N} mice with *Cx3cr1*-Cre^{ERT2} mice in which ERT2-fused Cre recombinase (CreERT2) is expressed under control of the macrophage-specific *Cx3cr1* promoter. Microglia-specific gene manipulation was achieved by exploiting the longevity of microglia. All experiments were conducted 4 weeks after tamoxifen treatment, a time when long-lived microglia retain the Nlrp3 D301N mutant, but peripheral monocytes have largely been replenished with newborn *Cx3cr1*-positive (*Cx3cr1*$^{+}$) cells with intact Nlrp3 expression. All mice were housed and maintained in the Laboratory Animal Resource Center of DGIST under standard conditions with *ad libitum* access to food and water. All animal procedures and experiments were performed in accordance with protocols approved by the Institutional Animal Care and Use Committee of DGIST (protocol number: DGIST-IACUC-23032704-0004). All experiments were conducted according to the guidelines and protocols for rodent experimentation approved by the Institutional Animal Care and Use Committee of DGIST.

Primary microglia culture

Cortices prepared from postnatal day 2–4 *Nlrp3*^{D301N}-cKI or control mouse pups were rinsed with ice-cold Hank's Balanced Salt Solution (HBSS) and incubated with 0.25% trypsin-EDTA for 15 min at 37°C with occasional inverting. Trypsin was inactivated by adding DMEM/F12 supplemented with 10% fetal bovine serum (FBS; Tissue Culture Biologicals) and 1% penicillin-streptomycin (Thermo Fisher). Trypsinized cortical tissues were subsequently dissociated by gentle pipetting and filtered through 70-μm cell strainers. Confluent mixed glia cultures were obtained by seeding cell suspensions onto 75-cm^2 flasks and maintaining them for approximately 21 days with regular media changes (twice a week). Microglia were isolated from confluent mixed glia cultures by mild trypsinization and plated onto poly-D-lysine–coated 0.4-μm–pore Transwell inserts (Costar).

Microglia-neuron co-culture using transwell

Isolated primary microglia (6×10^4) on poly-D-lysine–coated 0.4-μm–pore Transwell inserts were treated with 1 μM 4-hydroxytamoxifen (Cat# H7904; Sigma Aldrich) for 5 days to induce gene recombination. Thereafter, microglia cultures were rinsed with DMEM/F12 media and stimulated with LPS (0.25 μg/mL), or mock treated, for 3 h. Subsequently, Transwell inserts containing microglia were rinsed, and the culture medium within Transwell inserts was replaced with Neurobasal medium in which neuron cultures were grown. Prepared Transwell inserts were transferred to 24-well plates containing rat cortical neurons (3×10^5 cells/well). The resulting co-culture configuration allowed humoral communication between neuron culture and microglial culture through permeable membranes without physical contact. After 24 h, neuron cultures were analyzed by immunocytochemistry.

Culture, immunostaining, and image analysis of cultured neurons

Cortical neurons prepared from E18 rat embryonic brains were cultured on coverslips coated with poly-D-lysine and grown in Neurobasal medium supplemented with B-27 (Invitrogen), 0.5% FBS, 0.5 mM GlutaMax (Invitrogen) and sodium pyruvate (Invitrogen), as previously described.[57] At 13 days *in vitro* (DIV13), cultured neurons were incorporated into the Transwell co-culture system and maintained for 24 h. For immunostaining, neurons were fixed in 3.7% formaldehyde/4% sucrose in PBS, permeabilized with 0.2%

Triton X-100 in PBS, and blocked in PBS containing 3% horse serum and 0.1% BSA. Cells were then incubated with primary antibodies in the same blocking buffer for 1 h, followed by incubation with appropriate secondary antibodies. To label the surface NMDAR subunits, primary antibodies were incubated in 37°C for 10 min, prior to the fixation step. Fluorescence images were acquired using a confocal microscope (LSM800, Carl Zeiss) with a 63 × objective lens; all image settings were kept constant. z stack images were converted to maximal projection and analyzed to obtain the size and density of puncta immunoreactivities of marker proteins. Quantification was performed using MetaMorph software (Molecular Devices). For IL-1β treatment experiments, cultured neurons were exposed to human recombinant IL-1β (1 ng/mL) for 24 h, followed by immunostaining.

METHOD DETAILS

Drug administration

Tamoxifen (T5648; Sigma) was dissolved in corn oil and administered to 6-week-old mice by i.p. injection at a daily dose of 100 mg/kg for 5 days to induce Cre-mediated genetic knock-in. After allowing 4 weeks for peripheral monocyte replenishment, mice were intraperitoneally injected with 0.5 mg/kg LPS (from *Escherichia coli* O111:B4, L3012, Sigma, Lot# 12 170 308) or phosphate-buffered saline (PBS) twice at a 24-hour-interval. Mice were administered the NMDA receptor antagonist, memantine (M9292; Sigma), at 10 mg/kg (dissolved in PBS) or saline at the appropriate volume 30 min prior to all behavioral tests and/or histological analyses. Administration of recombinant interleukin (IL)-1 receptor antagonist (IL-1RA; at 10 mg/kg) started a day prior to the first behavioral tests and/or histological analysis.

Immunohistochemistry

Mice were deeply anesthetized by inhalation of isoflurane and immediately perfused, first with PBS for 3 min and then with 4% paraformaldehyde for 5 min. Brains were dissected, fixed in 4% paraformaldehyde overnight, and sliced into 40-μm-thick coronal sections using a vibratome (VT1200S; Leica). Brain sections were permeabilized by incubating with 0.2% Triton X-100 in PBS containing 5% bovine serum albumin and 5% horse serum for 1 h at room temperature. For immunostaining, brain sections were incubated for 16 h at 4°C with primary anti-Iba-1 (1:400), anti-CD68 (1:300), anti-GFP (1:500), anti-VGLUT1 (1:300), anti-PSD-95 (1:300), anti-VGAT (1:500), anti-$GABA_AR\gamma2$ (1: 1000), anti-GFAP (1:4000), or anti-S100β (1:300) antibodies, diluted in the same blocking solution. Sections were washed three times in PBS and incubated with species-appropriate Cy3-or fluorescein isothiocyanate (FITC)-conjugated secondary antibodies (Jackson ImmunoResearch) for 2 h at room temperature. After three washes with PBS, sections were mounted onto glass slides (Superfrost Plus; Fisher Scientific) with Vectashield mounting medium (H-1200; Vector Laboratories). Images were acquired by confocal microscopy (LSM800 or LSM700; Zeiss). Synaptic puncta were quantified using MetaMorph software (Molecular Devices), and their density and average area were measured.

Analysis of microglia morphology

z stack images were acquired at 3-μm intervals over a 15-μm z-range using a confocal microscope (Zeiss LSM800) and converted into single-plane maximal intensity projection images using Zen2.6 Software (Zeiss). Microglia within z-projection images were counted, contoured manually, and analyzed with respect to size and co-localization percentage between Iba-1^+ signals and $CD68^+$ signals (calculated as Iba-1^+CD68^+ area/Iba-1^+ area) using MetaMorph software (Molecular Devices). Microglia in z-projection images were categorized as ramified cells, with small/round soma and highly arborized long processes (at least 3 times (on average), longer than the size of the cell body); bushy cells, with enlarged cell bodies and swollen/retracted processes (processes less than 3 times, but more than 1.5 times (on average), longer than the cell body); and ameboid cells, with condensed cell bodies and few or no processes. All Iba-1 immunostained maximal intensity projection images were first enhanced for skeleton analyses to visualize microglia processes under the same conditions. Images were then converted to binary images, skeletonized, and analyzed using the AnalyzeSkeleton plugin (http://imagejdocu.tudor.lu) in ImageJ software as previously described.[28]

TUNEL staining

Apoptotic cells were visualized in fixed brain section using a terminal deoxynucleotidyltransferase (TdT) dUTP-biotin nick-end labeling (TUNEL) kit (*In Situ* Cell DeathDetection Kit, TMR red; Roche) according to the manufacturer's instructions. Images were acquired using a confocal microscope (LSM800; Carl Zeiss). Positive control images were acquired from brain sections that were pre-treated with DNaseI (Sigma; AMPD1) for 1 h at 37°C prior to TUNEL staining.

Preparation of brain lysates and quantification of cytokine expression level

Whole lysates of the mouse cerebrum were prepared by homogenizing the tissue in lysis buffer (1% Triton X-100, 50 mM Tris, 150 mM NaCl) containing 1 mM $MgCl_2$, 1 mM $CaCl_2$, 1 μg/mL aprotinin, 1 μg/mL leupeptin, 1 μg/mL pepstatin, 5 mM phenylmethyl sulfonyl fluoride (PMSF), 1 mM Na_3VO_4, and 5 mM sodium fluoride (NaF). After incubation on ice for 1 h, the supernatants were collected after centrifugation at 12,500 × g for 20 min, and protein concentration was measured using the Bradford assay. Protein expression levels of various cytokines in brain lysates were quantified using the mouse IL-1β DuoSet ELISA kit (#DY401; R&D Systems) and Proteome Profiler Mouse Cytokine Array Kit (#ARY006; R&D Systems), according to the manufacturer's instructions.

Immunoblot analysis

Whole lysates of mouse cerebrum were prepared as described above and immunoblotted with the antibodies indicated in each figure legend. Western blot images were quantified using the ImageJ software (National Institutes of Health).

Quantitative reverse transcription polymerase chain reaction (RT-qPCR)

The mouse cerebrum was freshly harvested, and total RNA was extracted using TRIzol reagent (Invitrogen) according to the manufacturer's protocol. Briefly, brain tissues were incubated with 1 mL of TRIzol reagent at room temperature for 5 min. After phenol-chloroform extraction, RNA in the upper aqueous phase was isolated and precipitated using 2-propanol. Precipitated RNA pellets were washed twice with 75% ethanol in diethyl pyrocarbonate (DEPC)-treated water and dissolved in same. cDNA was synthesized from 500 ng of RNA by reverse transcription using a ReverTra Ace-α kit (Toyobo). qPCR was performed on a CFX96 Touch Real-Time PCR system (BioRad) using TB green qPCR master mix (Takara). All reactions were performed in duplicates, and the ubiquitously expressed *Gapdh* (glyceraldehyde 3-phosphate dehydrogenase) gene was used for normalizing the expression levels of cytokines in each sample. The following target genes were amplified using the indicated primer pairs: mouse *Il1b*, 5′-GGT GTG TGA CGT TCC CAT TA-3' (forward) and 5′-ATT GAG GTG GAG AGC TTT CAG-3' (reverse); mouse TNFα, 5′-TTG TCT ACT CCC AGG TTC TCT-3' (forward) and 5′-GAG GTT GAC TTT CTC CTG GTA TG-3' (reverse); mouse *Il2*, 5′-GTG CCA ATT CGA TGA TGA GTC A-3' (forward) and 5′-GGG CTT GTT GAG ATG ATG CTT T-3' (reverse). mouse *Il4*, 5′-GAA GAA CAC CAC AGA GAG TGA G-3' (forward) and 5′-TGC AGC TCC ATG AGA ACA C-3' (reverse); mouse *Csf2*, 5′-GGC CTT GGA AGC ATG TAG AGG-3' (forward) and 5′-GGA GAA CTC GTT AGA GAC GAC TT-3' (reverse); mouse *Trem1*, 5′-CTG GTG GTG ACC AAG GGT TC-3' (forward) and 5′-CTT GGG TAG GGA TCG GGT TG-3' (reverse); mouse *Cxcl1*, 5′-TGC ACC CAA ACC GAA GTC AT-3' (forward) and 5′-CTC CGT TAC TTG GGG ACA CC-3' (reverse); mouse *Cxcl2*, 5′-CCA ACC ACC AGG CTA CAG G-3' (forward) and 5′-GCG TCA CAC TCA AGC TCT G-3' (reverse); mouse *Cxcl9*, 5′-ATC TTC CTG GAG CAG TGT GG-3' (forward) and 5′-AGT CCG GAT CTA GGC AGG TT-3' (reverse); mouse *Cxcl10*, 5′-CCA AGT GCT GCC GTC ATT TTC-3' (forward) and 5′-GGC TCG CAG GGA TGA TTT CAA-3' (reverse); mouse *Cxcl11*, 5′-CTG CTC AAG GCT TCC TTA TGT T-3' (forward) and 5′-GCC GTT ACT CGG GTA AAT TAC AGA A-3' (reverse); mouse *Timp1*, 5′-CAT GGA AAG CCT CTG TGG ATA TG-3' (forward) and 5′-AAG CTG CAG GCA CTG ATG TG-3' (reverse); mouse *P2ry12,* 5′-CAT TGC TGT ACA CCG TCC TG-3' (forward) and 5′-AAC TTG GCA CAC CAA GGT TC-3' (reverse); and mouse *Gapdh*, 5′-ACA TGG TCT ACA TGT TCC AG-3' (forward) and 5′-TCG CTC CTG GAA GAT GGT GAT-3' (reverse).

Preparation and titration of AAVs

HEK293T cells were co-transfected with pHelper, AAV1.0 vectors and pAAV-CW3SLhSyn-PSD95-mCherry-eGFP (ExPost) or pAAV-CW3SLhSyn-gephyrin-mCherry-eGFP (InhiPost). Cells were harvested 72 h later, lysed, and mixed with 40% polyethylene glycol and 2.5 M NaCl, and centrifuged at 2,000 × g for 30 min. The resulting pellets were resuspended in HEPES buffer (20 mM HEPES, 115 mM NaCl, 1.2 mM $CaCl_2$, 1.2 mM $MgCl_2$, 2.4 mM KH_2PO_4), mixed with an equal volume of chloroform, and centrifuged at 400 × g for 15 min. The supernatants were concentrated with a Amicon Ultra centrifugal filter (Millipore; UFC9030) at 3,600 × g for 20 min and then with an Amicon Ultra centrifugal filter (Millipore; UFC5003) at 14,000 × g for 10 min. Infectious titers of viruses were measured by RT-qPCR detection of eGFP sequences, with reference to a standard curve generated using the corresponding DNA plasmid.

Stereotaxic injections

Mice were anesthetized by inhalation of isoflurane (2–3%) and their heads were fixed by firmly securing to a stereotactic device. Virus solutions were injected into the hippocampal CA1 region using a NanoFil syringe and Nanoliter 2010 Injector (World Precision Instruments) at a flow rate of 0.1 μL/min. The coordinates used for the CA1 region of the dorsal hippocampus were AP -2.1 mm and ML ± 1.3 mm; the site at DV -1.5 mm received a 400-nL injection. Injected mice were allowed to recover for 14 days following surgery before i.p. administration of LPS.

Behavioral analysis

All behavioral tests were conducted in a dimly lit (< 5 lux), sound-proof room and analyzed using Noldus EthoVision software, unless specified otherwise. The sequence of behavioral tests was designed to minimize potential carryover effects of the preceding assay. Mice were habituated to the test room for at least 30 min prior to tests. (1) Open-field test. Mice were placed in a white-colored acrylic chamber (40 × 40 × 40 cm) for 30 min for assessment of general locomotor activity. The total distance traveled by freely moving mice was measured. (2) Ultrasonic vocalization test. Ultrasonic vocalizations (USVs) of male mice were promoted by housing the mice singly in individual cages for 48 h. On the day of the test, mice were acclimated to the soundproof recording chamber with red lighting for 5 min after which USVs were induced by introducing an anesthetized 6-week-old female into the chamber. The vaginal estrous condition of each stimulus female was assessed through visual inspection. Mouse vocalizations were recorded using Avisoft Recorder software and analyzed with Avisoft SASLab Pro (Avisoft Bioacoustics). (3) Marble burying test. Mice were introduced to standard cages filled with wood chip bedding (5 cm deep) without marbles for a 30-min habituation period. After habituation, mice were removed from the cages, and 15 marbles were placed on the surface of the bedding arranged in five rows of three (3 × 5). Mice were then returned to the cages and allowed to explore for 30 min, after which mice were again removed and the number of marbles buried approximately 3/4 deep within the bedding was counted. (4) 3-Chamber sociability test. This test used a white

acrylic box, divided into three chambers (20 × 40 × 22 cm each) with small openings on the dividing walls; both side chambers contained wire cups in the corners for enclosing social conspecifics. The subject mouse was placed in the middle chamber and allowed to freely explore the chambers for 10 min. After this habituation session, an age-matched social conspecific was introduced into the wire cup on the left side chamber, and the sociability of subjects was assessed by measuring their exploration times for the enclosed conspecific and empty cup during a second 10-min period. An exploration was counted when the subjects directed their nose near the wire cups. In the last 10 min, a new social conspecific was introduced into the empty wire cup on the right-side chamber, and social recognition was assessed by measuring the subject's exploration times for the familiar and novel conspecific in the wire cup. (5) Light/dark box test. This test employed a setup consisting of two interconnected chambers: a roofless, brightly illuminated chamber (> 200 lux) and a closed, dark chamber. The chambers were connected by a small entrance that allows free travel between them. The time spent in each chamber and the number of transitions were measured. (6) Novelty-suppressed feeding test. This test used an open-field plastic box (40 × 40 × 40 cm) with standard bedding, with a platform containing food pellets placed in the center of the field. Mice were food-deprived for 24 h to promote the exploration of novel environments. On the day of the test, mice were introduced to the testing box and allowed to travel and eat food pellets freely for 10 min. Mice were then transferred to their home cage, and their food consumption was measured for 10 min. Feeding latency and the number of feedings were assessed by measuring the subject's exploration time for the food pellet on the platform.

Cloning of IL-1β and IL-1RA for expression in *E. coli*

The recombinant plasmids for the mature form of human IL-1β (residues Ala117-Ser269) with an N-terminal 6 × His tag and human IL-1RA, codon-optimized for E. coli expression, were constructed using overlapping oligonucleotides, subcloned into the *NdeI* and *XhoI* sites of the pET28a and pET21a vectors (Novagen), respectively, and confirmed by DNA sequencing (BIOFACT). The validated clones were transformed into E. coli BL21 (DE3) RIL strain for protein expression. The cells were cultured in LB medium containing ampicillin (100 mg/mL) and chloramphenicol (50 mg/mL) at 37°C. After the culture reached an OD_{600} of 0.6–0.8, 1 M IPTG was added to a final concentration of 0.5 mM, and the culture was incubated at 37°C for 4 h to induce protein expression.

Purification of IL-1β and IL-1RA

For preparation of IL1Ra, a cell pellet was resuspended in lysis buffer (50 mM Tris-HCl (pH 7.5), 150 mM NaCl, 1 mM PMSF, 0.25% Tween 20 [v/v]) and the suspension was subjected to ultrasonic disruption using a Q700 Sonicator. The supernatant solution was subjected to buffer exchange using Dialysis Buffer (20 mM Tris-HCl [pH 7.5]). The wt-IL-1RA was loaded onto a HiTrap Q HP 5 mL column (GE Healthcare) equilibrated with binding buffer (20 mM Tris-HCl [pH 7.5]), which was then washed with the same buffer. Protein elution was achieved by gradually increasing the salt concentration from 10 mM to 1 M NaCl. The concentrated protein was injected into a HiLoad 16/60 Superdex 75 pg column (GE Healthcare) equilibrated with 20 mM phosphate buffer containing 150 mM NaCl (pH 7.4). For preparation of IL-1β, a cell pellet was resuspended in 50 mM Tris-HCl (pH 8.0), 500 mM NaCl, 1 mM PMSF, and 0.2% Tween 20, and disrupted by sonication on ice. The supernatant was loaded to a HisTrap HP 5 mL column (GE Healthcare) with wash buffer (50 mM Tris-HCl (pH 8.0), 500 mM NaCl) and eluted with a buffer containing 50 mM Tris-HCl (pH 8.0), 500 mM NaCl, and 250 mM imidazole. The protein fractions were dialyzed with 20 mM Tris-HCl, pH 7.5, loaded to a HiTrap HP Q 5 mL column (GE Healthcare), and washed with 20 mM Tris-HCl (pH 7.5). The protein was eluted by gradually increasing the salt concentration from 10 mM to 1 M. The eluate was concentrated and injected to a HiLoad 16/60 Superdex 75 pg column (GE Healthcare) in 20 mM sodium phosphate buffer containing 150 mM NaCl (pH 7.4).

Coimmunoprecipitation assays

Mouse brain synaptosomal fractions from P56 mice were extracted using deoxycholate, incubated with anti-IL1R1 overnight at 4°C, mixed with 30 μL of a 1:1 suspension of protein A-Sepharose (Incospharm Corp.), and incubated for 2 h at 4°C with gentle rotation. More specifically, mouse brains (1 g) were homogenized in 10 mL of ice-cold homogenization buffer consisting of 320 mM sucrose, 5 mM HEPES-NaOH (pH 7.5), 1 mM EDTA, 0.2 mM PMSF, 1 μg/mL aprotinin, 1 μg/mL leupeptin, 1 μg/mL pepstatin, and 1 mM Na_3VO_4. The homogenized tissue was centrifuged at 2,000 × *g* for 15 min, and the resulting supernatant was centrifuged at 100,000 × *g* for 1 h. The pellets were homogenized in buffer consisting of 20 mM HEPES-NaOH (pH 7.5), 0.15 M NaCl, 2 mM $CaCl_2$, 2 mM $MgCl_2$, 0.2 mM PMSF, 1 μg/mL aprotinin, 1 μg/mL leupeptin, 1 μg/mL pepstatin, and 1 mM Na_3VO_4. The pellet was dissolved by adding Triton X-100 to a final concentration of 1% (w/v) and performing constant stirring at 4°C for 1 h. Supernatants obtained after centrifugation at 100,000 × *g* for 1 h were used for coimmunoprecipitation assays. The beads were pelleted and washed three times with lysis buffer (20 mM HEPES-NaOH (pH 7.5), 0.15 M NaCl, 2 mM $CaCl_2$, 2 mM $MgCl_2$, 1% Triton X-100, 0.2 mM PMSF, 1 μg/mL aprotinin, 1 μg/mL leupeptin, 1 μg/mL pepstatin, and 1 mM Na_3VO_4). Immune complexes were resolved by SDS-PAGE and immunoblotted with the indicated antibodies.

Biotinylation assays

Cultured rat cortical neurons were treated with 1 ng/mL of IL-1β for 24 h and harvested at DIV14. The cells were then washed twice with ice-cold PBS, incubated with 1 mg/mL SulfoNHS-LC-biotin (Pierce) in ice-cold PBS for 30 min on ice, rinsed briefly with 0.1 M glycine in PBS, and incubated with 0.1 M glycine in PBS for 10 min at room temperature to completely quench the biotin reaction. The cells were then lysed with lysis buffer (1% Triton X-100, 0.1% SDS, 50 mM Tris (pH 7.4), 150 mM NaCl, and protease inhibitors) and

incubated for 30 min on ice. Cell debris was removed by centrifugation, 250 μg of lysate was incubated with 30 μL streptavidin agarose beads (Pierce) for 2 h at 4°C, the beads were washed thrice with lysis buffer, and the surface-labeled proteins were eluted with 2 × sample buffer and analyzed by immunoblotting using the indicated antibodies.

Flow cytometry

After euthanizing the mice, transcardial perfusion with cold PBS was performed to flush out circulating blood cells. The brain tissue was then carefully dissected, with the olfactory regions, brainstem, and meninges removed. Next, the brain tissue was homogenized in RPMI-1640 supplemented with DNase I and Collagenase IV. Following incubation at 37°C, the homogenized tissue was filtered through a 70 μm cell strainer. To remove myelin debris, the homogenates were subjected to Percoll gradient centrifugation, and the resulting single-cell suspension was prepared for flow cytometry analysis. Fluorochrome-conjugated monoclonal antibodies against CD45 (BioLegend, 103116), CD11b (Invitrogen, 12-0112-82), Ly6C (Biolegend, 128031), and Ly6G (Invitrogen, 17-9668-82) were used to stain the cells for flow cytometry analysis. To exclude dead cells, counterstaining was performed using 4′,6-diamidino-2-phenylindole (DAPI) (Invitrogen, D1306). Flow cytometry analyses were conducted using a FACS LSR Fortessa (BD Biosciences), and data were processed with FlowJo software (TreeStar).

Ex vivo electrophysiological recordings

Male mice were anesthetized with isoflurane and decapitated to remove the brains. The brains were quickly transferred and sectioned in an ice-cold slicing solution (3.3 mM KCl, 1.3 mM NaH_2PO_4, 26 mM $NaHCO_3$, 11 mM D-glucose, 211 mM sucrose, 0.5 mM $CaCl_2$ and 10 mM $MgCl_2$). Horizontal slices (300 μm) were prepared using a vibrating-knife microtome VT1000s (Leica Microsystems). Slices were stabilized for at 30°C for least 1 h in an oxygenated (95% O_2/5% CO_2) artificial cerebrospinal fluid (aCSF; 124 mM NaCl, 3.3 mM KCl, 1.3 mM NaH_2PO_4, 26 mM $NaHCO_3$, 11 mM D-glucose, 2 mM $CaCl_2$ and 1 mM $MgCl_2$). Slices were transferred to the recording chamber and perfused in an oxygenated (95% O_2/5% CO_2) artificial cerebrospinal fluid solution (aCSF). Patch electrodes (3–8MΩ) were prepared with capillary glass (Warner Instruments, USA) using a micropipette puller (P-97, Sutter Instrument, CA). Intra-pipette solution containing (in mM): 145 mM CsCl, 5 mM NaCl, 10 mM HEPES, 10 mM EGTA, 4 mM Mg-ATP, and 0.3 mM Na-GTP, adjusted to pH 7.3 with CsOH was used for the measurement of miniature inhibitory postsynaptic currents (mIPSCs) and miniature excitatory postsynaptic currents (mEPSCs). The osmolarity of the internal solution was 280–290 mOsm. Cells were voltage-clamped at −70 mV. The mIPSCs were isolated by blocking Na^+ channels, NMDARs, and AMPARs with bath-applied tetrodotoxin (TTX, 1 μM), D-2-amino-5-phosphonopentanoate (D-AP5, 50 μM) and cyanquixaline (CNQX, 10 μM), respectively. The mEPSCs were isolated by blocking Na^+ channels and $GABA_A$ receptors by bath-applying TTX (1 μM) and picrotoxin (PTX, 50 μM), respectively. Intra-pipette solution containing (in mM): 130 mM Cs-methanesulfonate, 5 mM TEA-Cl, 8 mM NaCl, 0.5 mM EGTA, 10 mM HEPES, 4 mM Mg-ATP, 0.4 mM Na-GTP, 1 mM QX-314 and 10 mM disodium phosphocreatine was used for the measurement of evoked EPSCs (eEPSCs) and NMDA-eEPSCs. The osmolarity of the internal solution was 280–290 mOsm. Electrical stimulation was applied using a concentric bipolar electrode (FHC). The bipolar electrode was placed in layer 2/3 of mPFC. The eEPSCs were recorded at −70 mV (for AMPAR-eEPSCs) and +40 mV (for NMDAR-eEPSCs; 50 ms after stimulation). To obtain the input/output (I/O) responses, the EPSCs were elicited by a series of stimulation intensities (20–100 μA). Two pulses at different intervals (50, 100, 200, and 500 ms) were delivered to calculate paired-pulse ratios (PPRs). PTX (50 μM) was applied to block the $GABA_A$ receptors for eEPSC recordings, and PTX (50 μM) and CNQX (10 μM) were applied to block the $GABA_A$ receptors and AMPARs, respectively, to record NMDAR-eEPSCs. Intra-pipette solution containing (in mM): 130 K-gluconate, 20 KCl, 0.2 EGTA, 10HEPES, 4 Mg-ATP, 0.3 Na-GTP, 10 Disodium phosphocreatine was used for the excitability recording. Current clamp recordings were performed by injecting current into mPFC layer 2/3 pyramidal neurons. The intensity per cell was varied from 0 to 250 pA in 25-pA increments into mPFC layer 2/3 pyramidal neurons. All recordings were performed using a Multiclamp 700B amplifier and DigiData 1550B digitizer (Molecular Devices). Only cells with access resistance (Ra) in the range of 5 MΩ < Ra <30 MΩ were analyzed.

In vitro electrophysiological recordings from cultured neurons

Cultured cortical neurons at DIV 14 were used. Using a Model P-97 pipette puller, pipettes were pulled from borosilicate glass (i.d., 0.86 mm; o.d., 1.5 mm; Sutter Instruments). The resistance of patch pipettes containing an internal solution ranged from 3 to 6 MΩ. Internal solutions vary according to experimental conditions, as followings: 145 mM CsCl, 0.3 mM Na-GTP, 10 mM EGTA, 10 mM HEPES, 5 mM NaCl, and 4 mM Mg-ATP, with pH adjusted to 7.2 to 7.4 with CsOH and an osmolarity of 290–295 mOsmol/L for mEPSCs and puffing application of NMDA and AMPA; 130 mM Cs-$MeSO_4$, 5 mM TEA-Cl, 1 mM QX-314, 0.5 mM EGTA, 8 mM NaCl, 10 mM HEPES, 0.4 mM Na-GTP, 10 mM disodium phosphocreatine, and 4 mM ATP-Mg, with pH adjusted to 7.2 to 7.4 with CsOH and an osmolarity of 290–295 mOsmol/L for recording NMDAR-eEPSCs and AMPAR-eEPSCs. The external solution included 130 mM NaCl,1 mM $MgCl_2$, 2 mM $CaCl_2$, 4 mM KCl, 10 mM D-glucose, and 10 mM HEPES with a pH of 7.2–7.4 calibrated with NaOH and an osmolarity of 300 to 305 mOsmol/L. The whole-cell arrangement was built at room temperature using M-TSC manipulators (SENSAPEX). Electrophysiological data were obtained using an Axon Multiclamp 700B amplifier and pCLAMP software and then digitized using an Axon DigiData 1550B data capture board (Axon Instruments). For puffing applications, NMDA and

AMPA were supplied directly to the dendrite area of the patched neurons at a puffing pressure of 6–8 psi, using a PV-820 Pneumatic PicoPump device (World Precision Instruments). Amplitudes were quantified and charge transfers were calculated over the 10-s period following the puff application. We recorded mEPSCs, puffing applications of AMPA, and AMPAR-eEPSCs at a holding potential of −70 mV, and recorded NMDA puffing and NMDAR-eEPSCs at a holding potential of +40 mV. Synaptic currents were analyzed offline using the Clampfit 10.8 software (Molecular Devices). For recording of mEPSCs, we added 1 μM TTX and 50 μM PTX to the external solution to block Na^+ currents and $GABA_A$ receptors, respectively. For recording of NMDAR-eEPSCs, 10 μM PTX and 10 μM CNQX were included in the extracellular solution, and for puffing applications of NMDA, 1 μM TTX was additionally included. Similarly, for recording AMPAR-eEPSCs, 10 μM PTX and 50 μM D-AP5 were included in the extracellular solution, and for puffing applications of AMPA, 1 μM TTX was added.

QUANTIFICATION AND STATISTICAL ANALYSIS

Quantification of 3D microglial engulfment

For analysis of microglial engulfment, z stack images were acquired at 1-μm intervals over a 20-μm z-range using a confocal microscope (Zeiss LSM800) with a 40 × objective. Images were analyzed by three-dimensionally reconstituting $EYFP^+$/$CD68^+$ microglial lysosomes using the "Surface" function of Imaris software (Oxford Instruments). Engulfed synaptic puncta within microglial lysosomes were defined by masking the PSD95 channel using the resulting microglial lysosome surface rendering. $PSD\text{-}95^+$ synaptic puncta within microglial surfaces were detected and quantified using the "Spots" function.

Analysis of microglial engulfment using a synapse engulfment reporter virus

For analysis of microglial engulfment using a reporter virus, the indicated reporter viruses were injected into the hippocampal CA1 of mice according to the timeline depicted in Figure 4F. Mice were sacrificed 6 days after LPS-injection and processed for immunohistochemical analysis. Brain sections containing hippocampal CA1 regions infected with the virus were immunostained for Iba1 and stained with AF647. z stack images were acquired at 5-μm intervals over a 15-μm z-range using a confocal microscope (Zeiss LSM800) with a 40 × objective. and converted into single-plane maximal intensity projection images using Zen2.6 Software (Zeiss). The content of engulfed synaptic material in microglia was quantified using MetaMorph software (Molecular Devices). Thresholded signals of mCherry, eGFP, and AF647 (Iba1) channels were used to measure three values: the total areas of $mCherry^+$ signals alone within $Iba1^+$ microglia, mCherry-$eGFP^+$ signals, or $Iba1^+$ microglia, respectively. The total area of $mCherry^+$ alone puncta within $Iba1^+$ microglia was normalized to the total area of $mCherry^+eGFP^+$ positive puncta and the total area of $Iba1^+$ microglia within the region of interest to compensate for the potentially different expression levels of adeno-associated virus (AAV) reporters and the potential difference in density of microglia, respectively.

Statistical analysis

All data are presented as means ± standard error of the mean (SEM). The normality of data distributions was evaluated using the D'Agostino & Pearson test. Data were statistically assessed using a Mann-Whitney *U* test, student's t-test, and ordinary one/two-way analysis of variance (ANOVA) followed by post hoc Tukey's test, Dunnett test, or Kruskal-Wallis test, as appropriate. Prism8.0 (GraphPad Software) was used to analyze data and prepare bar graphs. *p*-values < 0.05 were considered statistically significant.

Sample sizes (n) and statistical methods in each figure are as follows:

Figures 1E–1L: Control/*n* = 8; *Nlrp3*^{D301N}-cKI/*n* = 7, $^{**}p < 0.01$, $^{***}p < 0.001$, Mann–Whitney U-test; Figure 1N: Control/n = 7–8; Nlrp3^{D301N}-cKI/n = 6–7, $^{**}p < 0.01$, Mann–Whitney *U*-test. Figures 1P–1Q: Control/*n* = 35; Nlrp3^{D301N}-cKI/*n* = 46, Student's t-test; Figures 1R and 1S: Control/*n* = 39; Nlrp3^{D301N}-cKI/*n* = 43, $^{****}p < 0.0001$, Student's t-test; Figures 1T–1Z: Control/*n* = 19–23; Nlrp3^{D301N}-cKI/*n* = 19–26, $^{**}p < 0.01$, $^{***}p < 0.001$, $^{****}p < 0.0001$, Student's t-test; Figures 2B, 2D and 2F: Control/n = 9–13; Nlrp3^{D301N}-cKI/n = 8–14, $^{*}p < 0.05$, $^{**}p < 0.01$, Mann–Whitney *U*-test; Figures 2H and 2J: Ctrl+saline/*n* = 15–18, *Nlrp3*^{D301N}-cKI+saline/*n* = 14–17, Ctrl+Mem./*n* = 16–18, *Nlrp3*^{D301N}-cKI+Mem./*n* = 16–19, $^{*}p < 0.05$, $^{**}p < 0.01$ vs. Ctrl+saline group; $^{\#\#\#}p < 0.001$, $^{\#\#\#\#}p < 0.0001$ vs. *Nlrp3*^{D301N}-cKI+saline group, two-way ANOVA with the Tukey multiple comparison test; Figure 2M: Ctrl+saline/*n* = 17, *Nlrp3*^{D301N}-cKI+saline/*n* = 17, Ctrl+Mem./*n* = 17, *Nlrp3*^{D301N}-cKI+Mem./*n* = 15, $^{*}p < 0.05$ vs. Ctrl+saline group, $^{\#\#}p < 0.01$ vs. *Nlrp3*^{D301N}-cKI+saline group, two-way ANOVA with the Tukey multiple comparison test; Figure 3C: SHANK/Unstim./Control/*n* = 23, SHANK/Unstim./*Nlrp3*^{D301N}-cKI/*n* = 23, SHANK/LPS-treated Control/*n* = 23, SHANK/LPS-treated *Nlrp3*^{D301N}-cKI/*n* = 21, sGluN2A/Unstim./Control/*n* = 20; sGluN2A/Unstim./*Nlrp3*^{D301N}-cKI/*n* = 21; sGluN2A/LPS-treated Control/*n* = 21, sGluN2A/LPS-treated *Nlrp3*^{D301N}-cKI/*n* = 20; sGluN2B/Unstim./Control/*n* = 25, sGluN2B/Unstim./*Nlrp3*^{D301N}-cKI/*n* = 27, sGluN2B/LPS-treated Control/*n* = 27, sGluN2B/LPS-treated *Nlrp3*^{D301N}-cKI/*n* = 24, $^{*}p < 0.05$, $^{***}p < 0.001$ vs. LPS-treated Control, One-way ANOVA with the Tukey multiple comparison test; Figure 3D: n = 3–4 mice/group, $^{*}p < 0.05$, Mann–Whitney *U*-test; Figures 3E and 3F: n = 4–8 mice/group, $^{*}p < 0.05$, $^{**}p < 0.01$, Mann–Whitney *U*-test; Figures 3G and 3H: control/*n* = 5, *Nlrp3*^{D301N}-cKI/*n* = 4, $^{*}p < 0.05$, Mann–Whitney *U*-test; Figure 4B: SHANK/Veh/*n* = 27, SHANK/IL-1β/*n* = 28, sGluN2A/Veh/*n* = 33, sGluN2A/IL-1β/*n* = 36, sGluN2B/Veh/*n* = 25, sGluN2B/IL-1β/*n* = 32, $^{*}p < 0.05$, $^{**}p < 0.01$, Student's t-test; Figure 4D: number of independent experiments, *n* = 5 for all experimental groups, $^{*}p < 0.05$, Student's t-test; Figure 4F: number of independent experiments, *n* = 4,

*$p < 0.05$, Mann–Whitney *U*-test; Figure 4H: Veh/$n = 18$, IL-1β/$n = 18$, ***$p < 0.001$, Mann–Whitney *U*-test; Figure 4J: Veh/$n = 25$, IL-1β/$n = 16$, *$p < 0.05$, **$p < 0.01$, Mann–Whitney *U*-test; Figures 4M and 4O: Ctrl+saline/$n = 13$–14, *Nlrp3*^{D301N}-cKI+saline/$n = 13$–16, Ctrl+IL-1RA/$n = 12$–13, *Nlrp3*^{D301N}-cKI+IL-1RA/$n = 13$, **$p < 0.01$, ***$p < 0.001$, ****$p < 0.0001$ vs. Ctrl+saline group, $^{\#}p < 0.05$, $^{\#\#\#}p < 0.001$ vs. *Nlrp3*^{D301N}-cKI+saline group, two-way ANOVA with Tukey's multiple comparison test; Figure 4Q: Ctrl+saline/$n = 18$, *Nlrp3*^{D301N}-cKI+saline/$n = 22$, Ctrl+IL-1RA/$n = 17$, *Nlrp3*^{D301N}-cKI+IL-1RA/$n = 22$, ***$p < 0.001$ vs. Ctrl+saline group, $^{\#\#}p < 0.01$ vs. *Nlrp3*^{D301N}-cKI+saline group, two-way ANOVA with Tukey's multiple comparison test.